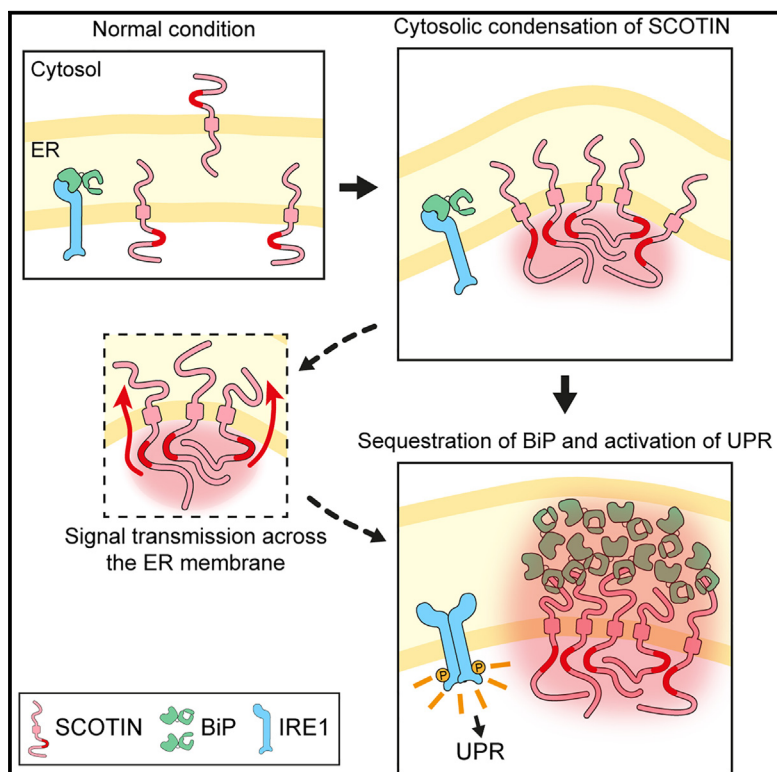


Membrane-tethered SCOTIN condensates elicit an endoplasmic reticulum stress response by sequestering luminal BiP

Graphical abstract



Authors

Areum Jo, Minkyo Jung, Ji Young Mun, Young Jin Kim, Joo-Yeon Yoo

Correspondence

jyoo@postech.ac.kr

In brief

Jo et al. demonstrated that SCOTIN condensates induce apoptosis and ER stress responses. The condensation of SCOTIN in cytosolic compartments transmits signals across the membrane, resulting in a structural transition in the luminal compartment. Sequestration of the ER chaperone BiP within SCOTIN condensates triggers ER stress responses.

Highlights

- SCOTIN condensates on the ER membrane activate ER stress responses
- The ER chaperone BiP is sequestered within immobile SCOTIN condensates
- Cytosolic condensation of SCOTIN is critical for BiP sequestration and UPR activation



Article

Membrane-tethered SCOTIN condensates elicit an endoplasmic reticulum stress response by sequestering luminal BiP

Areum Jo,¹ Minkyo Jung,² Ji Young Mun,² Young Jin Kim,¹ and Joo-Yeon Yoo^{1,3,*}

¹Department of Life Sciences, Pohang University of Science and Technology, Pohang, Republic of Korea

²Neural Circuit Research Group, Korea Brain Research Institute, Daegu 41062, Republic of Korea

³Lead contact

*Correspondence: jyoo@postech.ac.kr

<https://doi.org/10.1016/j.celrep.2025.115297>

SUMMARY

The endoplasmic reticulum (ER) stress response controls the balance between cellular survival and death. Here, we implicate SCOTIN, an interferon-inducible ER protein, in activating the ER stress response and modulating cell fate through its proline-rich domain (PRD)-mediated cytosolic condensation. SCOTIN over-expression leads to the formation of condensates enveloping multiple layers of the ER, accompanied by morphological signs of organelle stress. Luminal BiP chaperone proteins are sequestered within these SCOTIN condensates, which elicit ER stress responses. The colocalization of luminal BiP with SCOTIN is strictly contingent upon the PRD-mediated condensation of SCOTIN in the cytosolic compartment, closely associated with the ER membrane. The cysteine-rich domain (CRD) of SCOTIN, along with the condensation-prone PRD domain, is required for ER stress induction. We propose that membrane-associated condensation transduces signals across the ER membrane, leading to the induction of BiP assembly and the ER stress response.

INTRODUCTION

In eukaryotic cells, the endoplasmic reticulum (ER) functions as a central organelle crucial for protein synthesis, lipid metabolism, calcium storage, and vesicle trafficking. This vast organelle exhibits a sheet structure connected to the nuclear membrane and interconnected tubular structures in the periphery. Maintaining the highly dynamic structure and morphology of the ER is essential for the normal functions of diverse cellular processes.^{1,2} Under cellular stress conditions, the tubular ER often expands to increase the protein folding capacity and the biosynthesis of ER proteins and lipids.^{3,4} Environmental or intracellular conditions that disrupt the normal functions of the ER lead to ER stress, activating a set of integrated signaling pathways collectively called the unfolded protein response (UPR).^{5,6} The UPR is initiated by the activation of stress sensor proteins in the ER; namely, IRE1 α , PERK, and ATF6 α .⁷ Once activated, the UPR, in turn, results in the activation of molecular machineries for the transcriptional induction of chaperones, transient arrest of translation, ER-associated degradation (ERAD), and autophagy to remove unfolded proteins.^{8,9}

To prevent the damaging effects of protein aggregates, misfolded proteins in the ER, including secretory and membrane proteins, are removed by the protein quality control and degradation system; i.e., ERAD.^{10,11} ER-resident chaperones such as BiP, calnexin, and calreticulin aid in the proper folding and modification of newly synthesized proteins.^{12,13} Molecular ma-

chineries monitoring proper protein folding and trafficking in the ER are also closely linked to the protein quality control system, as demonstrated by the lysosomal degradation of misfolded transmembrane proteins confined within distinct ER-associated compartments.^{14–16} The accumulation of protein aggregates in the cytosol saturates the buffering capacity of molecular chaperones and factors of ERAD, such as p97.^{17–19} Consequently, misfolded and unfolded proteins accumulate on the luminal side of the ER, triggering the ER stress response. Generally, in correctly folded proteins, hydrophobic regions are buried within the protein core; in contrast, protein misfolding results in the exposure of hydrophobic motifs, promoting oligomerization and aggregation with other proteins.^{20,21} Proteins that form toxic aggregates often contain intrinsically disordered regions (IDRs), whose amino acid sequences encode structural instability and mobile flexibility.^{22,23}

SCOTIN is a single-pass ER transmembrane protein whose expression is induced under conditions of DNA damage or interferon stimulation.^{24,25} Its expression is reportedly required for apoptosis in γ -irradiated mouse fibroblasts²⁴ and for apoptosis in pancreatic β cells in obese mice.²⁶ However, the role of SCOTIN in the regulation of cell survival or death is unclear. Recent reports indicate that SCOTIN self-assembles and condenses in a manner dependent on its intrinsically disordered C-terminal domain.^{27,28} During the observation of SCOTIN condensates along the ER membrane, severe alterations in ER morphology were also observed. This finding prompted an



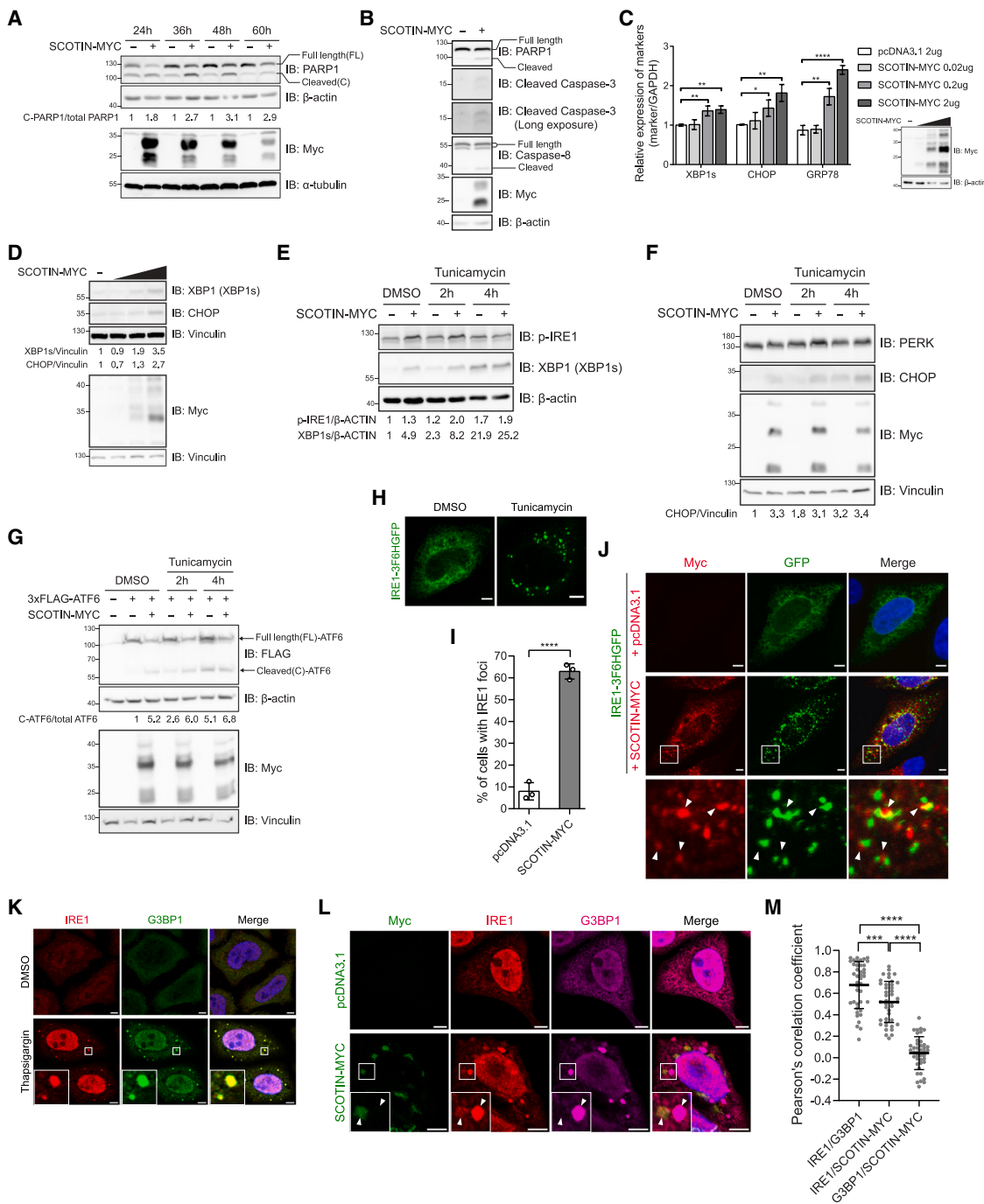


Figure 1. SCOTIN overexpression induces cell death and activates the ER stress response

- (A) PARP1 cleavage in HeLa cells expressing SCOTIN-MYC was evaluated by western blotting at the indicated times after transfection. See also Figure S1B.
- (B) Cleavage of PARP1, caspase-3, and caspase-8 following SCOTIN-MYC overexpression was evaluated by western blotting 24 h after transfection.
- (C) The mRNA levels of XBP1s, CHOP, and GRP78 in HeLa cells expressing SCOTIN-MYC were measured by RT-qPCR. The protein levels of SCOTIN-MYC were measured by western blotting. The error bars indicate the means ± SDs from triplicate experiments.
- (D) The protein levels of XBP1s and CHOP in HeLa cells expressing SCOTIN-MYC were measured by western blotting.
- (E-G) HeLa cells were transfected with the indicated constructs and treated with tunicamycin (1 µg/mL) for the indicated times before cell harvesting. Protein levels were measured by western blotting.
- (H) IRE1-3F6HGFP focus formation was induced by tunicamycin (1 µg/mL) treatment for 4 h in HeLa cells. Scale bars, 5 µm.
- (I) Statistical analysis of IRE1-3F6HGFP focus formation in SCOTIN-MYC-expressing HeLa cells. The graph presents the means ± SDs of three independent experiments.

(legend continued on next page)

investigation into whether and how SCOTIN condensates function in the ER stress response.

RESULTS

SCOTIN overexpression induces cell death and activates the ER stress response

As reported previously,^{24,26} HeLa cells overexpressing SCOTIN undergo apoptosis (Figure 1A). PARP1 cleavage, a hallmark of apoptosis, was detected 24 h post transfection, persisting even 60 h post transfection of SCOTIN-MYC. Moreover, 24 h after transfection, cleaved caspase-3 and caspase-8 were detected in SCOTIN-MYC-expressing cells (Figure 1B). Evaluation of cell viability using a 3-(4,5-dimethylthiazol-2-yl)-2,5-diphenyltetrazolium bromide assay and trypan blue staining confirmed a reduction in the number of viable cells in SCOTIN-MYC-transfected cells compared to that in control vector-transfected cells (Figures S1A and S1B).

SCOTIN, when overexpressed, assembles into condensates along the ER membrane, as reported previously.²⁸ This assembly is accompanied by alterations in ER morphology. Given the occurrence of apoptosis in SCOTIN-overexpressing cells, we sought to determine whether the presence of SCOTIN condensates on the ER membrane triggers any markers of ER stress. To investigate this hypothesis, the UPR was directly examined by measuring the production of the spliced form of XBP1 (XBP1s), the induction of CCAAT-enhancer-binding protein homologous protein (CHOP), and the expression of ER chaperones such as BiP (also known as GRP78) in SCOTIN-overexpressing cells (Figures 1C and 1D). The data clearly demonstrated that these UPR markers were significantly elicited in response to the overproduction of SCOTIN-MYC. Consequently, the activation of the ER stress sensor proteins IRE1 α , PERK, and ATF6 α was examined in SCOTIN-overexpressing cells (Figures 1E–1G). SCOTIN-MYC overexpression alone was sufficient to induce the phosphorylation of IRE1 α , reduce PERK mobility, and induce the cleavage of ATF6.

To determine the extent to which the ER stress response was activated by SCOTIN overexpression, cells were treated with tunicamycin, a known inducer of ER stress, for 2 or 4 h, and the results were compared with those in cells transfected with the control vector alone or with SCOTIN-MYC (Figures 1E–1G). In control vector-transfected cells, robust activation of the UPR was observed after 4 h of tunicamycin treatment, as evidenced by the phosphorylation of IRE1 α , cleavage of ATF6, production of XBP1s, or induction of CHOP. Notably, SCOTIN overexpression alone elicited significant activation of the UPR comparable to that induced by tunicamycin. Moreover, tunicamycin treatment did not result in augmented activation of the UPR in SCOTIN-overexpressing cells, suggesting that the pathways activated by tunicamycin treatment and SCOTIN overexpression overlap and likely involve the same ER stress sensors.

To visualize the activation of the UPR in SCOTIN-expressing cells, the oligomerization of IRE1 α was monitored by confocal fluorescence microscopy using the IRE1-3 \times FLAG-6 \times Histidine-GFP (IRE1-3F6HGFP) construct. IRE1 α oligomerization induced by tunicamycin was visualized as distinct GFP foci²⁹ (Figure 1H). In contrast to the findings in cells treated with tunicamycin, in which IRE1 foci were detected in almost every tested cell, approximately 63% of SCOTIN-MYC-expressing cells exhibited IRE1 foci (Figure 1I). This result indicates that IRE1 oligomerization is indeed induced in SCOTIN-MYC-expressing cells but that the UPR is not activated in all SCOTIN-MYC-expressing cells. Interestingly, cells with IRE1 foci tended to also contain SCOTIN puncta. Notably, the IRE1 foci were positioned near the SCOTIN puncta, with some partially overlapping but not completely colocalizing (Figure 1J).

Recent studies have shown that the assembly of IRE1 foci is coupled to stress granule (SG) formation.³⁰ To investigate whether SCOTIN-induced IRE1 foci are associated with SGs, we examined endogenous IRE1 and G3BP1 in cells expressing SCOTIN-MYC. Consistent with a previous report, endogenous IRE1 colocalized with SG following thapsigargin treatment (Figure 1K). Among SCOTIN-punctum-forming cells, approximately 34% formed G3BP1 puncta (Figure 1L). While not all SCOTIN-MYC-expressing cells formed G3BP1 puncta, in those that did, G3BP1 puncta colocalized with IRE1. However, consistent with our previous observation, these IRE1(+)/G3BP1(+) puncta did not colocalize with SCOTIN puncta (Figures 1M and S3A). These findings suggest that overexpressed SCOTIN can indirectly link SGs to IRE1.

SCOTIN condensation is critical for inducing ER stress

Upon detecting IRE1-3F6HGFP foci in cells with SCOTIN puncta, we investigated whether the assembly of SCOTIN condensates on the ER membrane is necessary for the activation of the ER stress response. To investigate this possibility, we examined the SCOTIN(Δ 150–177)-MYC mutant, which cannot condense.²⁸ To eliminate potential interference from endogenous SCOTIN, we compared the effects of reconstitution with full-length SCOTIN and reconstitution with the SCOTIN mutant with deletion of amino acids (aa) 150–170 on the ER stress response in SCOTIN knockout (KO) HeLa cells.

First, we investigated the production of XBP1s and the induction of CHOP in SCOTIN(Δ 150–177)-MYC-transfected cells. In contrast to SCOTIN-MYC overexpression, SCOTIN(Δ 150–177)-MYC overexpression barely induced the UPR (Figure 2A). Next, we compared the number of IRE1 foci resulting from SCOTIN overexpression. Significantly fewer IRE1 foci were detected in SCOTIN(Δ 150–177)-MYC-overexpressing cells than in SCOTIN-MYC-overexpressing cells, confirming that SCOTIN(Δ 150–177)-MYC overexpression barely induces IRE1 oligomerization or the UPR (Figures 2B and 2C).

(J) Representative confocal images of IRE1-3F6HGFP focus formation in SCOTIN-MYC-expressing HeLa cells. Scale bars, 5 μ m.

(K) Confocal images of IRE1 and G3BP1 in HeLa cells. The IRE1 cluster and SG were induced by thapsigargin (50 μ M) treatment for 1 h. Scale bars, 5 μ m.

(L) Confocal images of SCOTIN-MYC, IRE1, and G3BP1 in HeLa cells. Scale bars, 5 μ m.

(M) Quantification data for colocalization of IRE1/SCOTIN-MYC, IRE1/G3BP1, and SCOTIN-MYC/G3BP1 in (L) ($n = 41$). The error bars indicate the means \pm SDs. See also Figure S3A.

The asterisks indicate the p values determined by an unpaired two-tailed t test. * $p < 0.05$, ** $p < 0.01$, *** $p < 0.001$, **** $p < 0.0001$.

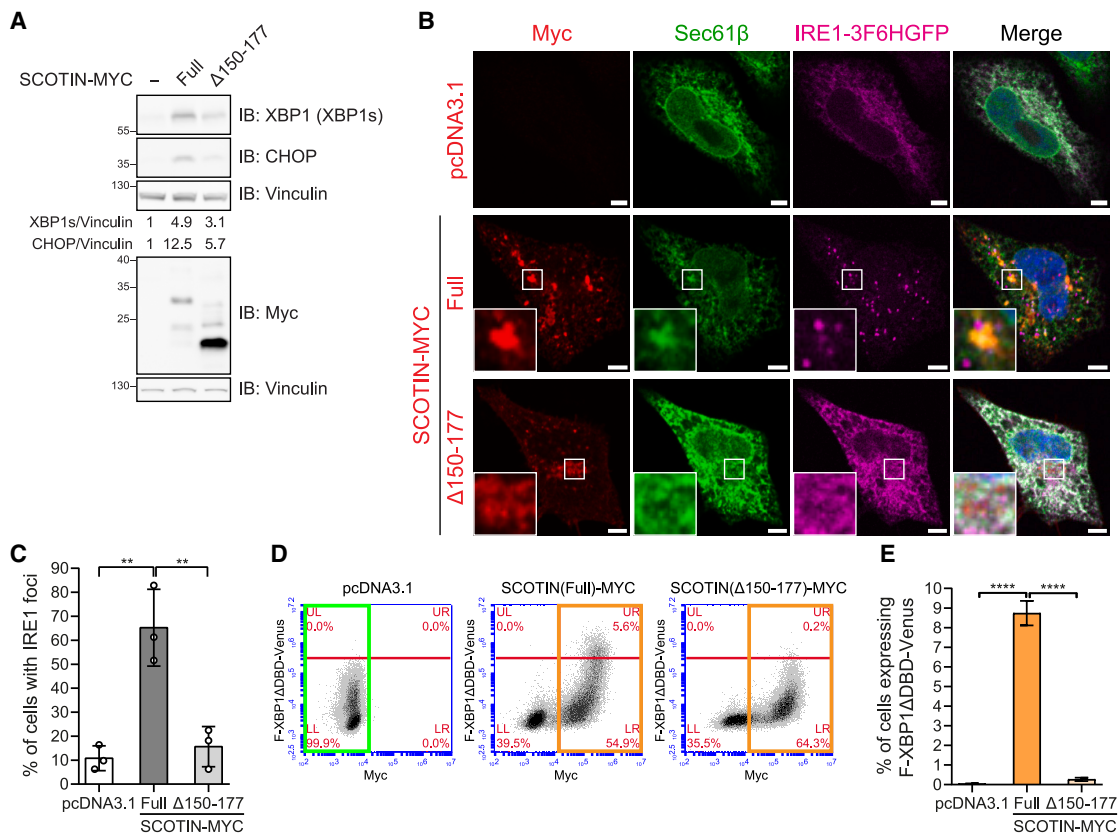


Figure 2. SCOTIN condensation is critical for inducing ER stress

(A) The production of XBP1s and induction of CHOP in SCOTIN KO HeLa cells expressing SCOTIN(full)-MYC or SCOTIN(Δ150–177)-MYC were evaluated by western blotting.

(B) Representative confocal images of IRE1-3F6HGFP focus formation in SCOTIN KO HeLa cells expressing SCOTIN(full)-MYC or SCOTIN(Δ150–177)-MYC. Scale bars, 5 μm.

(C) Statistical analysis of IRE1-3F6HGFP focus formation in SCOTIN KO HeLa cells expressing SCOTIN(full)-MYC or SCOTIN(Δ150–177)-MYC. The graph presents the means ± SDs of three independent experiments.

(D) Images of representative flow cytometry density plots showing the production of F-XBP1ΔDBD-Venus in SCOTIN KO HeLa cells expressing SCOTIN(full)-MYC or SCOTIN(Δ150–177)-MYC.

(E) Statistical analysis of the F-XBP1ΔDBD-Venus production data in (D). The error bars indicate the means ± SDs from triplicate experiments. The asterisks indicate the *p* values determined by an unpaired two-tailed t test. **p* < 0.05, ***p* < 0.01, ****p* < 0.001, *****p* < 0.0001.

To quantify UPR activity in SCOTIN-overexpressing cells, we monitored the splicing of XBP1 at the single-cell level using the FLAG-XBP1ΔDBD-Venus (F-XBP1ΔDBD-Venus) construct. Upon activation of the UPR, the IRE1α endoribonuclease excises a 26 bp segment within the XBP1 mRNA in the cytosol, thereby generating the spliced form of XBP1 mRNA.^{31,32} The F-XBP1ΔDBD-Venus construct was developed to monitor the activity of IRE1α, as the translation of the Venus protein occurs only after the splicing of XBP1 mRNA.³³ In cells cotransfected with SCOTIN-MYC and F-XBP1ΔDBD-Venus, we analyzed the production of Venus relative to SCOTIN expression by flow cytometry. The basal level of Venus expression was negligible and not affected by empty vector transfection. Venus was produced in approximately 8.7% of SCOTIN-MYC-expressing cells, indicating that XBP1 splicing occurred (Figures 2D and 2E). However, the production of F-XBP1ΔDBD-Venus by SCOTIN was abolished when SCOTIN(Δ150–177)-MYC was transfected.

Based on these results, we concluded that the ability of SCOTIN to condense on the ER is essential for activation of the UPR.

Morphological signs of cellular stress in cells with SCOTIN condensates

After observing the activation of the ER stress response, we investigated the ultrastructure of the ER near SCOTIN puncta. Our previous investigation employing correlative light and electron microscopy (CLEM) analysis of cells expressing SCOTIN-DsRed revealed the coexistence of entangled ER membranes and SCOTIN condensates.²⁸ Furthermore, open cytosolic spaces surrounded by curved ER membranes were noted.²⁸ Considering the potential impact of this large globular fluorescent protein on molecular interactions within the condensates, we reinvestigated the ultrastructure of ER regions associated with SCOTIN puncta utilizing a reasonably small tag that allows the fusion to mimic the natural conformation. To achieve this

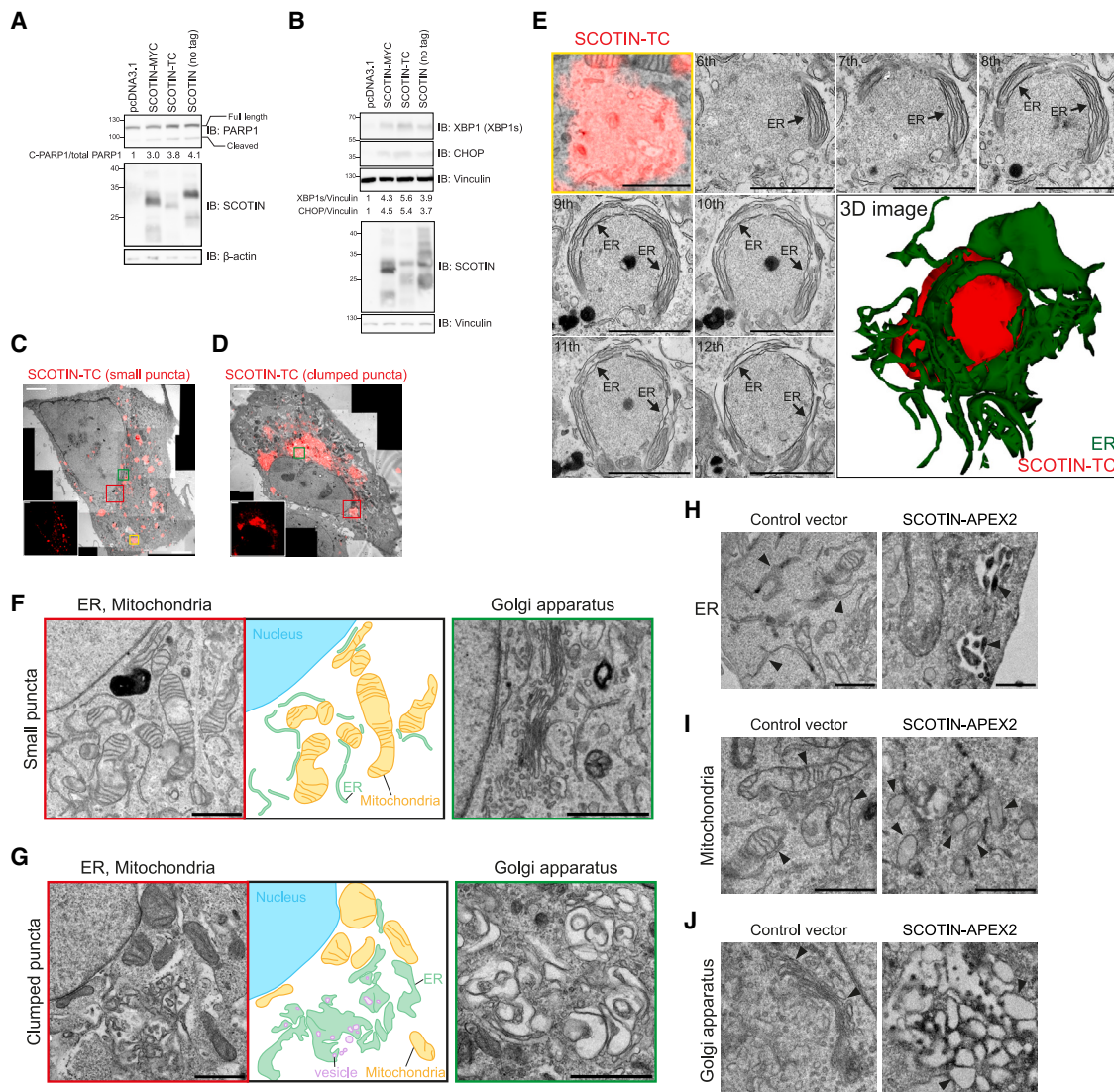


Figure 3. Morphological signs of cellular stress in cells with SCOTIN condensates

(A and B) HeLa cells were transfected with MYC-tagged, TC-tagged, or untagged SCOTIN. PARP1 cleavage (A) and production of XBPs1s and induction of CHOP (B) were evaluated by western blotting.

(C and D) CLEM images of HeLa cells expressing SCOTIN-TC. Scale bars, 5 μm.

(E) Enlarged image of SCOTIN-TC puncta in the yellow box in (C). The 3D distribution of SCOTIN-TC was determined by reconstruction from 18 serial images. Scale bars, 1 μm.

(F and G) Enlarged images of SCOTIN-TC puncta in the red box (ER and mitochondria) and green box (Golgi apparatus) in (C) and (D). Scale bars, 1 μm.

(H–J) TEM images of HeLa cells expressing SCOTIN-APEX2 or the control vector. Scale bars, 1 μm.

See also Figure S2.

goal, we used a tetracycline (TC) tag in combination with the fluorescent, membrane-permeable biarsenical dye ReAsH-EDT₂.³⁴

Similar to overexpression of MYC-tagged SCOTIN, overexpression of TC-tagged or non-tagged SCOTIN led to cell death, as evidenced by PARP1 cleavage (Figure 3A). Furthermore, overexpression of these triggered ER stress, as indicated by the production of XBPs1s or induction of CHOP (Figure 3B), suggesting that the induction of cell death or ER stress is an intrinsic ability of SCOTIN overexpression. Subsequently, live cells were

treated with ReAsH-EDT₂ to label SCOTIN-TC, and the ultrastructure of SCOTIN puncta was analyzed using CLEM (Figures 3C and 3D). Similar to the previous observations for overexpressed SCOTIN-MYC, irregularly shaped clumped structures of SCOTIN-TC puncta were observed along the ER membrane. Serial micrographs of SCOTIN-TC puncta were acquired simultaneously for three-dimensional (3D) reconstruction (Figures 3E and S2A; Video S1). The 3D reconstruction clearly demonstrated the spherical cores of SCOTIN-TC puncta surrounded by multiple strands of ER membranes. In addition,

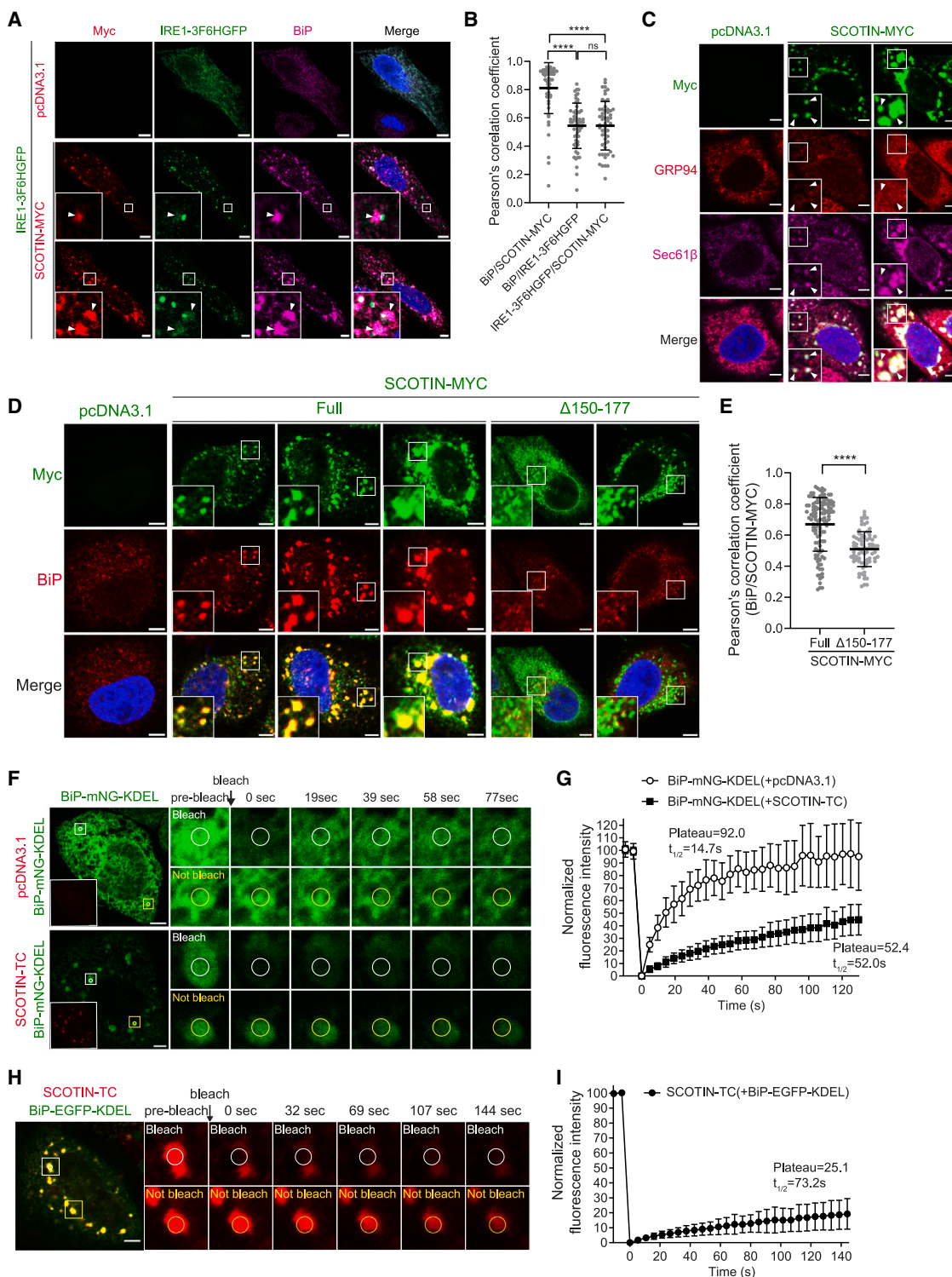


Figure 4. BiP, an ER chaperone protein, is sequestered within immobile SCOTIN condensates

(A) Confocal images of SCOTIN-MYC, IRE1-3F6HGFP, and BiP in HeLa cells. Scale bars, 5 μ m.

(B) Quantification data for colocalization of IRE1-3F6HGFP/BiP, IRE1-3F6HGFP/SCOTIN-MYC, and SCOTIN-MYC/BiP in (A) ($n = 56$). The error bars indicate the means \pm SDs. See also Figure S3B.

(C) Confocal images of SCOTIN-MYC, GRP94 and Sec61 β in HeLa cells. Scale bars, 5 μ m.

(D) Confocal images of BiP in SCOTIN KO HeLa cells expressing SCOTIN(full)-MYC or SCOTIN(Δ 150–177)-MYC. Scale bars, 5 μ m

(legend continued on next page)

relatively small SCOTIN-TC puncta were observed in the cytosolic space between organelles.

SCOTIN-TC puncta were frequently observed near organelles such as mitochondria, the Golgi apparatus, or vesicles in addition to the ER. Although the general organelle morphology in cells with relatively small SCOTIN-TC puncta appeared normal, similar to that in cells transfected with the control vector (Figures 3F and S2B), severe alterations in organelle structure, including ER dilation, mitochondrial fragmentation with collapsed cristae, and Golgi apparatus swelling, were observed in cells with larger clumped SCOTIN-TC puncta (Figure 3G). Trapped vesicles within the dilated ER were also detected.

In a separate analysis, we visualized the ultrastructure of SCOTIN-APEX2-overexpressing cells via transmission electron microscopy (TEM). APEX2 catalyzes the hydrogen peroxide-dependent conversion of 3,3'-diaminobenzidine into an insoluble polymer visible via electron microscopy upon treatment with osmium tetroxide.³⁵ We observed that the dark-stained fragmented ER was localized within cellular compartments surrounded by membranes, indicating the clearance of damaged ER (Figures 3H, S2D, and S2E). Moreover, abnormal morphological changes in intracellular organelles, such as mitochondrial fragmentation and Golgi apparatus swelling, were observed in SCOTIN-APEX2-expressing cells, indicating severe cellular stress (Figures 3I, 3J, and S2C–S2F).

BiP, an ER chaperone protein, is sequestered within immobile SCOTIN condensates

Upon observing the activation of the UPR, including the oligomerization of IRE1, by the presence of SCOTIN condensates, we sought to understand the mechanism underlying IRE1 oligomerization. Initially, we hypothesized that IRE1 might be directly activated by SCOTIN condensates, enabling its oligomerization. However, co-staining of IRE1 and SCOTIN disproved this hypothesis, as colocalization of IRE1 and SCOTIN puncta was rarely detected (Figure 1J).

Subsequently, we proposed an alternative hypothesis that a cellular component essential for controlling IRE1 oligomerization is sequestered in SCOTIN puncta. The dissociation of prebound BiP from IRE1 is a prerequisite for the oligomerization of IRE1 and other stress sensors.^{36,37} We therefore hypothesized that the selective sequestration of BiP within SCOTIN condensates might reduce the probability of its binding to IRE1, thereby promoting IRE1 oligomerization. To investigate this possibility, we examined the colocalization of endogenous BiP with SCOTIN condensates. SCOTIN-MYC puncta, ranging in size from small to large, colocalized with BiP near IRE1 foci (Figures 4A, 4B, and S3B). In contrast, colocalization of another ER chaperone protein, GRP94, with SCOTIN puncta was barely detected (Figure 4C), indicating a specific association between BiP and SCOTIN condensates. Furthermore, BiP rarely colocalized

with SCOTIN(Δ150–177)-MYC (Figures 4D, 4E, and S3C), indicating that PRD-mediated condensation is needed for their colocalization.

Given that BiP is a major chaperone protein that senses and binds misfolded proteins, its freely diffusing form serves as a marker to distinguish homeostatic ER from stressed ER.³⁸ To evaluate the availability of freely diffusing luminal BiP in SCOTIN-overexpressing cells, we transfected cells with BiP-(GGGGS)₃-mNeonGreen-KDEL (BiP-mNG-KDEL) and assessed its mobility using a fluorescence recovery after photobleaching (FRAP) assay (Figure 4F). In control vector-transfected cells, BiP-mNG-KDEL showed almost complete recovery after photo-bleaching. However, within SCOTIN puncta, its mobility was reduced approximately 3-fold (Figure 4G). Specifically, we calculated a diffusion coefficient of 0.0032 μm²/s in control cells and 0.0009 μm²/s within SCOTIN puncta.³⁸ Given the significant reduction in the molecular rearrangement rate of SCOTIN colocalized with BiP, we postulate that condensates containing both SCOTIN and BiP are immobile (Figures 4H and 4I).

PRD-mediated condensation is needed for physical interaction between SCOTIN and the luminal BiP

Observing colocalization of SCOTIN and luminal BiP, we hypothesized a physical interaction between the two proteins. To investigate this, we performed co-immunoprecipitation (coIP) experiments and confirmed that SCOTIN-MYC-expressing cells exhibited a clear physical interaction with endogenous BiP (Figure 5A). Given that luminal BiP recognizes and binds partially folded or unfolded protein substrates via its substrate binding domain (SBD),^{39–41} we sought to determine whether the SCOTIN-BiP interaction is mediated by the SBD. To this end, we utilized BiP^{V461F}-EGFP-KDEL, a mutant bearing a substrate binding-disrupting mutation at the valine 461 residue.⁴¹ No physical interaction between SCOTIN and BiP^{V461F} was observed, indicating that BiP likely recognizes and binds partially folded or unfolded regions of SCOTIN's luminal domain, specifically the cysteine-rich domain (CRD) (Figure 5B). Additionally, we examined the interaction of SCOTIN-MYC with BiP^{K294F}-EGFP-KDEL, a mutant bearing a dysfunctional mutation in the nucleotide binding domain.⁴¹ Interestingly, the interaction between SCOTIN-MYC and BiP^{K294F} was comparable to that observed with wild-type BiP, further supporting the role of the SBD in mediating the SCOTIN-BiP interaction (Figure 5B).

Under microscopy, no evident colocalization was observed between BiP and SCOTIN(Δ150–177) (Figure 4D). However, since the primary amino acid sequence of the luminal CRD in SCOTIN(Δ150–177) remains identical to that in SCOTIN, it is conceivable that BiP might still recognize and bind SCOTIN(Δ150–177) if the interaction is primarily mediated by the CRD. However, coIP analysis revealed no detectable physical interaction between SCOTIN(Δ150–177) and BiP (Figure 5C).

(E) Quantification data for colocalization of BiP/SCOTIN-MYC in (D) (SCOTIN(full)-MYC, n = 116; SCOTIN(Δ150–177)-MYC, n = 77). The error bars indicate the means ± SDs. See also Figure S3C.

(F and G) FRAP assay of BiP-(GGGGS)₃-mNeonGreen-KDEL (BiP-mNG-KDEL), which colocalizes with SCOTIN-TC, in HeLa cells (n = 23). The error bars indicate the means ± SDs.

(H and I) FRAP assay of SCOTIN-TC, which colocalizes with BiP-EGFP-KDEL, in HeLa cells (n = 16). The error bars indicate the means ± SDs.

The asterisks indicate the p values determined by an unpaired two-tailed t test. *p < 0.05, **p < 0.01, ***p < 0.001, ****p < 0.0001.

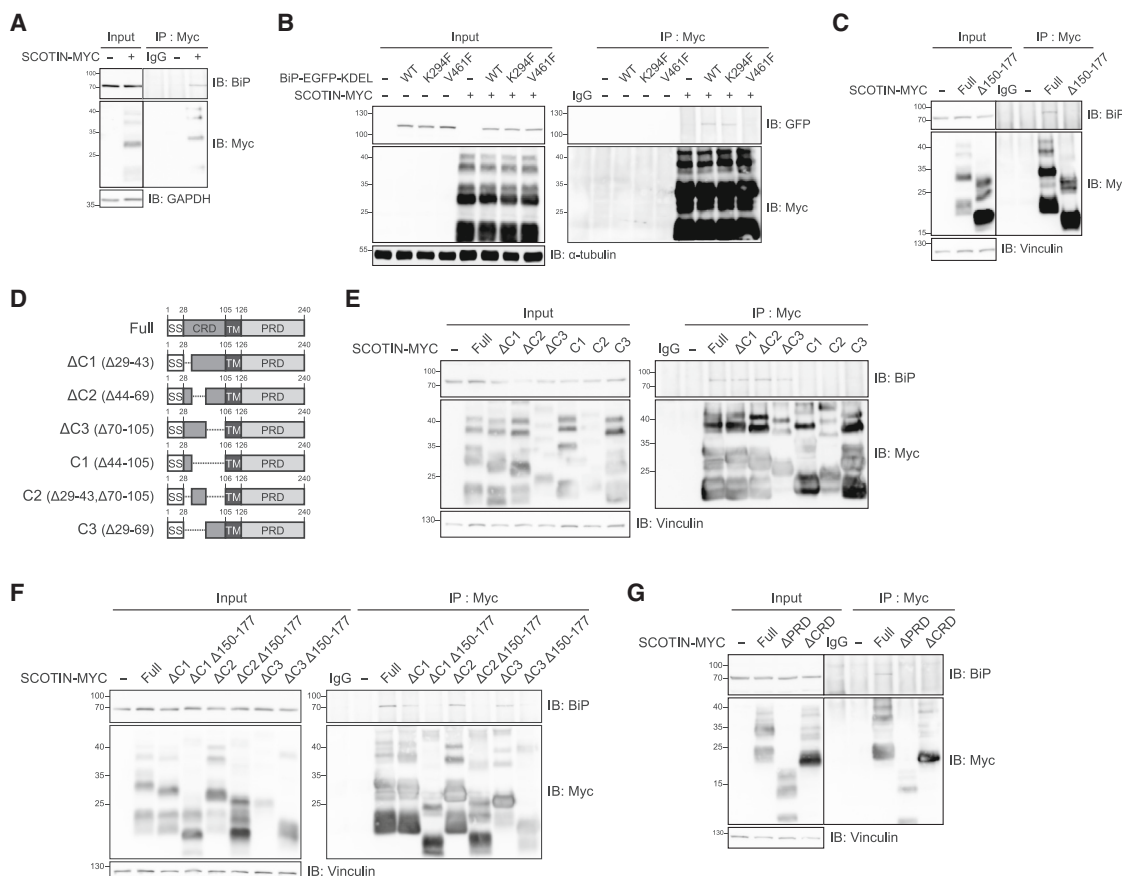


Figure 5. PRD-mediated condensation is needed for physical interaction between SCOTIN and the luminal BiP

- (A) Co-immunoprecipitation (coIP) of SCOTIN-MYC with endogenous BiP in HeLa cells.
- (B) CoIP of SCOTIN-MYC with BiP-EGFP-KDEL mutants in HeLa cells.
- (C) CoIP of SCOTIN(full)-MYC or SCOTIN(Δ150-177)-MYC with endogenous BiP in SCOTIN KO HeLa cells.
- (D) Schematic of the CRD deletion mutant constructs of SCOTIN-MYC.
- (E–G) CoIP of SCOTIN-MYC mutants with endogenous BiP in SCOTIN KO HeLa cells.

This result indicates that the partially unfolded structures in the CRD necessary for BiP SBD recognition rely on condensation in the cytosolic PRD.

To elucidate the luminal interactions between SCOTIN and BiP, we generated a series of SCOTIN CRD deletion mutants and assessed their ability to associate with BiP (Figure 5D). Mutants lacking one-third of the CRD (ΔC1, ΔC2, and ΔC3) maintained interactions with BiP comparable to that of SCOTIN with an intact CRD (Figures 5E). In contrast, mutants lacking two-thirds of the CRD (C1, C2, and C3) failed to interact (Figure 5E). Notably, introducing an additional deletion of the 150- to 177-aa region to ΔC1, ΔC2, or ΔC3 mutant abolished their interactions with BiP (Figure 5F). Moreover, truncation mutants of SCOTIN lacking either the CRD or PRD also failed to interact with BiP, underscoring the necessity of both domains being separated by the membrane to enable BiP-SCOTIN association (Figure 5G). Collectively, these observations suggest that the cytosolic condensation of SCOTIN, mediated by the PRD, is a prerequisite for its association with BiP in the luminal compartment. PRD-mediated condensation on the cytosolic side likely promotes

an aberrant structure transition in the luminal domain, facilitating recognition and binding by BiP.

PRD-mediated condensation and BiP sequestration are functionally linked to the induction of ER stress responses

Upon observing the colocalization and physical interaction of BiP and SCOTIN, we sought to determine whether these events are essential steps for subsequent activation of the ER stress response. To address this, we first investigated whether BiP colocalizes with the CRD mutants. Most CRD mutants formed punctate structures, as revealed by fluorescence microscopy (Figure 6A). Interestingly, endogenous BiP clearly colocalized with these punctate structures, regardless of the presence of physical interactions detected in coIP experiments (Figure 6B and S3D). Furthermore, the BiP^{V461F} mutant, which failed to interact with SCOTIN in coIP assays, also colocalized with SCOTIN puncta (Figure 6C). However, the formation of SCOTIN condensates on the ER membrane was a prerequisite for BiP sequestration within SCOTIN puncta. The deletion of

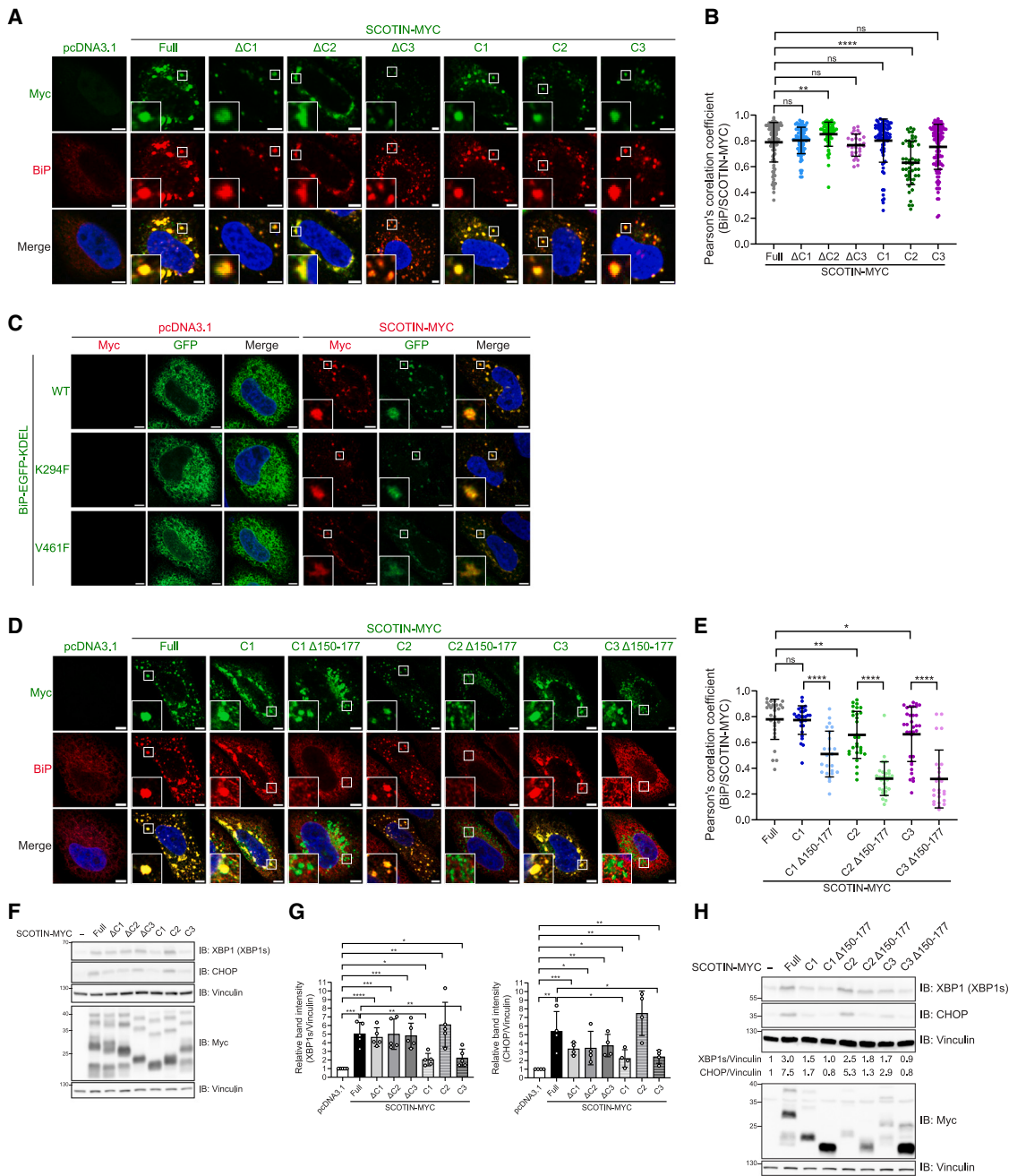


Figure 6. PRD-mediated condensation and BiP sequestration are functionally linked to the induction of ER stress responses

- (A) Confocal images of SCOTIN-MYC mutants and endogenous BiP in SCOTIN KO HeLa cells. Scale bars, 5 μ m.
- (B) Quantification data for colocalization of BiP/SCOTIN-MYC in (A) ($n = 30-119$). The error bars indicate the means \pm SDs. See also Figure S3D.
- (C) Confocal images of BiP-EGFP-KDEL mutants and SCOTIN-MYC in HeLa cells. Scale bars, 5 μ m.
- (D) Confocal images of SCOTIN-MYC mutants and endogenous BiP in SCOTIN KO HeLa cells. Scale bars, 5 μ m.
- (E) Quantification data for colocalization of BiP/SCOTIN-MYC in (D) ($n = 23-33$). The error bars indicate the means \pm SDs. See also Figure S3E.
- (F) Representative immunoblot image showing the protein levels of XBP1s and CHOP in SCOTIN KO HeLa cells expressing the indicated SCOTIN-MYC mutants.
- (G) Statistical analysis of the band intensities corresponding to the XBP1s and CHOP proteins. The graph of XBP1s shows the means \pm SDs of four independent experiments. The graph of CHOP expression presents the means \pm SDs of five independent experiments.
- (H) The production of XBP1s and induction of CHOP in SCOTIN KO HeLa cells transfected with the indicated SCOTIN-MYC mutants were evaluated by western blotting.
- The asterisks indicate the p values determined by an unpaired two-tailed t test. * $p < 0.05$, ** $p < 0.01$, *** $p < 0.001$, **** $p < 0.0001$.

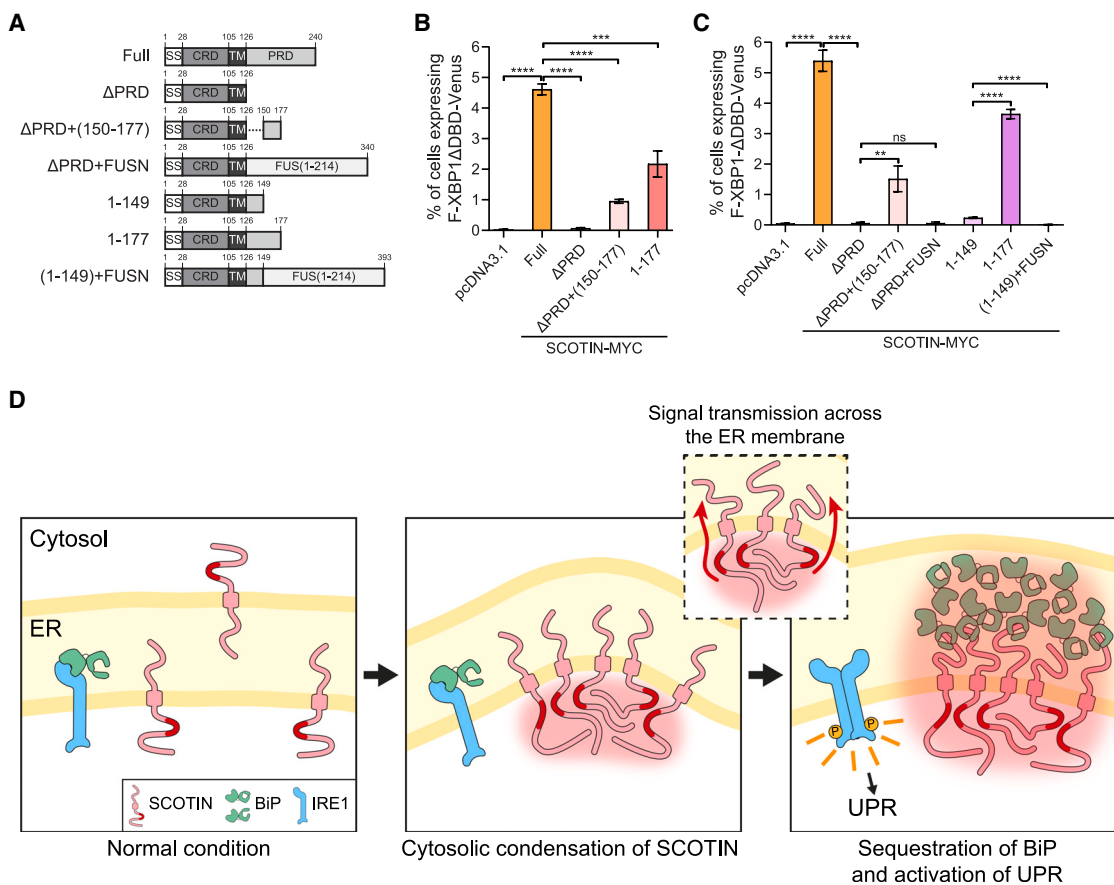


Figure 7. Cytosolic condensation of the SCOTIN PRD is essential for the induction of ER stress

(A) Schematic of the SCOTIN mutant constructs and chimeric constructs.

(B and C) Statistical analysis of F-XBP1 Δ DBD-Venus production in SCOTIN KO HeLa cells expressing the indicated constructs, as determined using flow cytometry. See also Figures S4A and S4B. The error bars indicate the means \pm SDs from triplicate experiments.

(D) Working model of membrane-tethered SCOTIN condensates eliciting an ER stress response by sequestering luminal BiP.

The asterisks indicate the p values determined by an unpaired two-tailed t test. * p < 0.05, ** p < 0.01, *** p < 0.001, **** p < 0.0001.

the internal 150- to 177-aa region in the C1, C2, and C3 mutants abolished their ability to form large condensates, which, in turn, eliminated colocalization with BiP (Figures 6D, 6E, and S3E).

To investigate the functional impact of these findings on the ER stress responses, we analyzed the production of XBP1s and the induction of CHOP in cells transfected with various SCOTIN CRD mutants (Figures 6F and 6G). In terms of XBP1s production, all tested mutants exhibited a level of XBP1 splicing comparable to the wild type, except for the C1 and C2 mutants, which showed relatively reduced effects. Similarly, for CHOP induction, the overall patterns were consistent across mutants. The most significant differences in ER stress activation were observed with the Δ 150-177 mutant (Figure 6H). In all cases (C1, C2, and C3), the addition of the Δ 150-177 mutation led to a marked reduction in both XBP1 and CHOP production, confirming that SCOTIN condensation via the cytosolic PRD is essential for BiP sequestration and induction of ER stress responses.

Our data thus far demonstrate that cytosolic condensation of the SCOTIN PRD results in the transduction of signals to the

luminal side of the ER, resulting in the sequestration of BiP within SCOTIN condensates, ultimately triggering the ER stress response. This phenomenon relies on the presence of the internal 150-177 aa of the SCOTIN PRD, which govern its condensation. We thus sought to determine whether the mere presence of the 150-177 aa is sufficient to induce ER stress. To investigate this possibility, we generated mutant constructs by adding the 150-177 aa to the SCOTIN(Δ PRD) or SCOTIN(1-149) mutant, neither of which could induce ER stress (Figures 7A–7C). We then quantified the proportions of cells expressing F-XBP1 Δ DBD-Venus, which serves as an indicator of the ER stress, among cells expressing full-length SCOTIN or SCOTIN mutants. Although adding 150-177 aa to the SCOTIN(Δ PRD) mutant resulted in a slight increase in the proportion of cells expressing F-XBP1 Δ DBD-Venus, it was insufficient for full restoration to a proportion comparable to that observed among cells expressing full-length SCOTIN (Figures 7B and S4A).

Finally, we investigated whether the cytosolic SCOTIN PRD could be replaced by other proteins with condensate-forming

potential to induce ER stress. To answer this question, we engineered mutant constructs of SCOTIN(Δ PRD) fused with 1–214 aa of FUS (FUSN). However, the fusion of FUSN with SCOTIN(Δ PRD)-MYC or SCOTIN(1–149)-MYC did not increase the production of F-XBP1 Δ DBD-Venus (Figures 7C and S4B). These data suggest that the intrinsic activity of the entire PRD of SCOTIN is necessary for activating the ER stress response.

DISCUSSION

Here, we demonstrated that the presence of SCOTIN condensates on the ER membrane induces ER stress through the sequestration of luminal BiP proteins within the condensates. Our data indicate that both the cytosolic PRD and the luminal CRD of SCOTIN are necessary to mediate condensation-mediated induction of ER stress (Figures S4C and S4D). Based on these observations, we propose that condensation of the PRD in the cytosolic compartment transmits signals across the membrane, leading to an aberrant CRD structural transition in the luminal compartment (Figure 7D). This structural change may be sufficient for the recruitment of BiP and activation of the ER stress response.

Following ligand-receptor interactions on the plasma membrane, a series of structural alterations occurs within the juxta-transmembrane and cytosolic domains of the receptors. These conformational changes facilitate the transduction of extracellular signals across the membrane into cytosolic compartments, leading to the activation of downstream signaling pathways. We propose that, analogous to the formation of signaling complexes on the cytosolic surface of the plasma membrane, membrane-associated condensation on the cytosolic surface of the ER membrane serves as a mechanism for transmitting signals into the ER lumen. This process results in BiP recruitment and the activation of ER stress responses.

While the assembly of most ligand-receptor interaction-mediated signaling complexes relies on specific protein-protein interactions, BiP's recognition and binding to substrate protein depends on hydrophobic regions exposed in misfolded or unfolded proteins.^{42,43} To explain the co-condensation of BiP with SCOTIN, we hypothesize three possible modes of interaction. First, a direct binding between the SCOTIN CRD and BiP SBD, as demonstrated in our coIP assays, may underlie the observed co-condensation. Second, structure alterations in the SCOTIN CRD induced by cytosolic condensation might expose hydrophobic regions, enabling their interaction with BiP. Finally, it is also possible that an adaptor protein specifically sequestered within the SCOTIN condensates mediates an indirect association between SCOTIN and BiP.

To find clues how SCOTIN forms a complex with BiP, we utilized AlphaFold2 (AF) to model SCOTIN with and without BiP. Although the AF model structures were not fully reliable due to the absence of the membrane component, they provide valuable insights into the interaction between the SCOTIN CRD and BiP SBD. The SBD is further divided into the β sandwich domain (β SBD), which contains the polypeptide-binding site and the α -helical domain (α Lid), which flexibly transitions between open and closed states depending on the substrate.^{44,45} BiP exhibits two primary functional conformations: the ATP-bound

state, characterized by a domain-docked conformation, and the ADP-bound state, characterized by a domain-undocked conformation with a high affinity for substrates.^{46–49} Since the ADP-bound state of BiP resembles the Apo state, we modeled SCOTIN with BiP using the SBD in its apo state (Figure S5A).

In the AF model of the SCOTIN CRD, we identified that the C1 and C2 regions formed antiparallel β sheets stabilized by disulfide bond bridge, while the C3 region was disordered (Figure S5B). The complex revealed that the C1 and C2 regions are positioned near BiP's β SBD, the α Lid, or concavity between them. In contrast, the disordered C3 region appear to pass through the polypeptide-binding pocket in the β SBD, corresponding to our experimental observation that SCOTIN fails to interact with the BiP^{V461F} mutant, which harbors a substrate binding-disrupting mutation (Figure S5C). Additionally, the predicted conformation of BiP in the SCOTIN-BiP complex closely resembled known structures of peptide-bound BiP and peptide-bound DnaK, a prokaryotic Hsp70 family protein^{46,50} (Figure S5D). The high-confidence prediction is supported by structural alignment data, where the $C\alpha$ root-mean-square deviation between the BiP AF model and DnaK is 1.089 Å and that between the BiP AF model and BiP structure is 1.176 Å, validating the use of AF for predicting interaction between two proteins. This prediction also aligned well with the established mechanism of the cofactors of Hsp70-family proteins. For example, nucleotide exchange factors, with their unstructured N-terminal domains, regulate BiP activity by directly binding to the polypeptide-binding site or displacing substrates from the β SBD of BiP.^{51,52}

To investigate the influence of SCOTIN PRD, as observed in the coIP assay (Figure 5F), we examined the AF model structures of SCOTIN CRD mutants with and without PRD as well as their interactions with BiP. We compared the structures of SCOTIN full-length and SCOTIN CRDTM, which was depleted of PRD. Most SCOTIN CRD mutants exhibited partial folding or more disorder, a characteristic that persisted regardless of PRD depletion (Figure S5E). Additionally, in the SCOTIN-BiP complex, the protein fold was poorly maintained in the absence of the PRD (Figure S5F). These predictive data suggest that the cytosolic PRD is essential for proper folding of the SCOTIN and its recognition by BiP.^{51,52}

Given that the association between BiP and the luminal SCOTIN CRD is contingent upon cytosolic PRD-mediated condensation, we sought to investigate whether the assembly of the cytosolic PRD might trigger the assembly, or even the condensation, of the CRD attached to the membrane on the luminal side. To this end, we conducted experiments to determine whether the CRD can undergo liquid-liquid phase separation by employing mCherry-labeled Cry2 optoDroplet assay systems. While the mCherry-Cry2 protein alone can multimerize upon blue light exposure, its ability to do so is limited. However, when this protein was fused with the IDR of FUS, HNRNPA1, or DDX4, rapid cluster assembly and phase separation, occurring in a manner dependent on blue light exposure, have been reported in cells.⁵³ Thus, using this assay system, we examined whether the CRD of SCOTIN facilitates blue-light-dependent assembly of mCherry-Cry2 similar to that observed with FUS-IDR. Upon blue-light exposure, a significant proportion of the cells

expressing CRD-mCherry-Cry2 exhibited droplet-like assembly structures (Figures S6A and S6B). Notably, live-cell microscopy revealed both fusion and fission of the CRD-mCherry-Cry2 droplets, suggesting their liquid-like nature. Although these data suggest the potential for phase separation of the SCOTIN CRD, we lack direct evidence of CRD phase separation within the ER lumen in cells. Furthermore, we lack direct evidence to assert that this phase separation behavior of the CRD contributes to the assembly of SCOTIN with BiP or the induction of ER stress. However, whether condensation signals are transduced across the membrane remains an intriguing question.

The heat shock response in the cytosol and nucleus and the UPR in the ER are key mechanisms that are activated under stress condition to maintain proteostasis.^{5,54} Various heat shock proteins are involved in the assembly and disassembly of molecular condensates during these responses.^{55,56} Upon stress, the heat shock-specific transcription factor HSF1 forms condensate to promote transcription of target genes.^{57,58} The chaperone HSP70 regulates transcription by disrupting the condensation and liquid-to-gel phase transition of HSF1.^{57,58} Moreover, HSP70 and the co-chaperone Sis1 maintain the orphan ribosomal protein condensates in a liquid-like state, preventing their solidification while ribosome biogenesis is blocked.⁵⁹ SGs are another form of stress-induced condensates composed of mature proteins and RNA.⁶⁰ The role of HSP90 in the assembly dynamics of SGs and processing bodies is well characterized.^{61–63} HSP90 is also required for the resolution of SGs through interactions with their components, as exemplified by its interaction with DYRK3.⁶⁴ Furthermore, HSP90 is required for maintaining the liquid-like state of the purinosome, an assembly of purine biosynthetic enzymes.⁶⁵

In contrast, the small heat shock protein HSP27 interacts with the oligomeric form of p62 on damaged lysosomes, facilitating its condensation and promoting lysophagy.⁶⁶ HSP27 also functions during the phase separation of cytoplasmic TDP-43, inhibiting the phase transition from a liquid to a gel-like or solid state.⁶⁷ Similarly, the phase transition of FUS is modulated by several heat shock proteins, including HSP27, DNAJB1, and HspB8.^{68–70} Recent studies have also revealed links between SGs and the UPR signaling pathway.^{30,71} However, the role of chaperones in regulating condensates in the UPR remains poorly understood. Here, we report the close association of BiP, a member of the eukaryotic Hsp70 family of proteins, with SCOTIN condensates. Unlike other heat shock proteins, which regulate assembly dynamics, BiP-SCOTIN condensates are immobile. This immobility results in a deficiency of the freely diffusing form of luminal BiP, thereby triggering activation of the UPR.

There are two conceivable explanations for the formation of immobile BiP-SCOTIN condensates. First, BiP may recognize and bind to immobile SCOTIN condensates on the ER membrane. Second, the association of BiP with the luminal domain of SCOTIN might facilitate its transition to an immobile state. In both cases, the presence of assembled SCOTIN condensates on the ER membrane is a prerequisite for BiP association. Given that SCOTIN is an interferon-stimulated protein with an antiviral function,²⁵ we hypothesize that the abnormal conformation of assembled SCOTIN on the ER membrane is likely perceived as

a stress signal. However, further studies are warranted to elucidate how BiP functions as a chaperone in SCOTIN condensates or how SCOTIN involves the activity of BiP.

SCOTIN is a multifunctional protein predominantly active under stress conditions. Initially, it was identified as a regulator of apoptosis in γ -irradiated mouse fibroblasts in a p53-dependent manner as well as in pancreatic β cells in obese mice.^{24,26} Additionally, SCOTIN has been implicated in autophagic degradation processes in hepatitis C virus (HCV)-infected cells.²⁵ Our research further reveals that SCOTIN condensates on the ER membrane induce ER stress. The concentration of SCOTIN is critical for the formation and dynamics of condensates, controlling their assembly and disassembly. Notably, SCOTIN is an inducible protein, upregulated under conditions such as interferon-mediated inflammatory responses or γ -irradiation-induced DNA damage.^{24,25} Moreover, high SCOTIN expression in cancer patients is often associated with a poor prognosis, suggesting a potential link between its expression and physiological roles.²⁸ To explore the role of SCOTIN in UPR signaling during physiological or therapeutic processes, particularly in interferon-induced apoptosis, we investigated the function of endogenous SCOTIN under these conditions. Given the variability in endogenous SCOTIN levels, its inducibility by interferon, and the extent of interferon-induced apoptosis across different cell lines, we first screened various cell lines for apoptosis inducibility upon interferon treatment (Figures S7A and S7B). However, apoptosis induced solely by interferon proved challenging to detect within the time frame of small interfering RNA knockdown experiments. To address this, we also tested UV irradiation, as SCOTIN condensation has been associated previously with DNA damage.²⁸ Among the 13 cell lines tested, apoptosis induced by interferon and UV irradiation was significantly impaired by SCOTIN knockdown in Huh7 and U-2 OS cells (Figures S7C and S7D). Huh7, a hepatocyte-derived carcinoma cell line in which HCV inhibition by SCOTIN has been reported previously,²⁵ showed strong inducibility of endogenous SCOTIN protein by interferon γ (IFN γ). In contrast, U-2 OS, an osteosarcoma-derived cancer cell line, exhibited a higher basal SCOTIN protein level compared to other cell lines.

We hypothesized that, under cellular stress conditions, SCOTIN levels reach a threshold necessary for condensation. SCOTIN appears to exist in diffuse, condensed, or aggregated states on the ER membrane, reflecting its expression status and physiological roles. These different states may correspond to its distinct functional roles, including the regulation of secretion, protein degradation, induction of the ER stress response, and even cell death. We propose that SCOTIN condensate formation serves as a defense mechanism, maintaining cellular homeostasis under stress conditions by maintaining the balance between cell survival and death.

Limitations of the study

One limitation of this study is the inability to visualize endogenous SCOTIN without tagging due to the unavailability of a commercial antibody suitable for immunofluorescence or immunoprecipitation. Furthermore, while we primarily assessed the role of overexpressed, tagged SCOTIN introduced via transfection in HeLa cells, as presented throughout the study except

Figure S7, it is important to acknowledge significant heterogeneity observed across various cell lines in terms of basal SCOTIN levels, its inducibility upon interferon treatment, and the extent of apoptosis induced by stimuli such as IFN and DNA-damaging agents.

RESOURCE AVAILABILITY

Lead contact

Requests for further information, resources, and reagents should be directed to and will be fulfilled by the lead contact, Joo-Yeon Yoo (jyoo@postech.ac.kr).

Materials availability

Plasmids generated in this study will be made available upon request.

Data and code availability

This paper does not report original code. Any additional information required to reanalyze the data reported in this paper is available from the [lead contact](#) upon request.

ACKNOWLEDGMENTS

This work was supported by National Research Foundation of Korea (NRF) grants funded by the Korean government (MSIT): NRF-2017R1A5A1015366 and RS-2023-00260454. This research was supported by the KBRI basic research program through Korea Brain Research Institute funded by Ministry of Science and ICT (24-BR-01-03). TEM data were acquired at Brain Research Core Facilities in KBRI.

AUTHOR CONTRIBUTIONS

M.J. performed CLEM and TEM experiments. A.J. performed all other experiments. All of the authors participated in the data analysis and discussions. A.J. and J.-Y.Y. wrote the manuscript with input from M.J., J.Y.M., and Y.J.K.

DECLARATION OF INTERESTS

The authors declare no competing interests.

STAR METHODS

Detailed methods are provided in the online version of this paper and include the following:

- **KEY RESOURCES TABLE**
- **EXPERIMENTAL MODEL AND STUDY PARTICIPANT DETAILS**
 - Cell culture and transfection
 - SCOTIN knockout cell generation with CRISPR-Cas9-mediated genome editing
- **METHOD DETAILS**
 - Plasmid construction
 - RNA isolation and reverse transcription-quantitative polymerase chain reaction (RT-qPCR)
 - Immunoblotting
 - Co-immunoprecipitation (coIP)
 - Immunostaining for fluorescence microscopy
 - FRAP assay
 - Correlative light and electron microscopy (CLEM) and 3D reconstruction
 - Transmission electron microscopy (TEM)
 - Flow cytometry
 - MTT assay
 - optoDroplet assay
 - Protein structure prediction using AlphaFold2
- **QUANTIFICATION AND STATISTICAL ANALYSIS**

SUPPLEMENTAL INFORMATION

Supplemental information can be found online at <https://doi.org/10.1016/j.celrep.2025.115297>.

Received: June 21, 2024

Revised: January 10, 2025

Accepted: January 21, 2025

Published: February 12, 2025

REFERENCES

1. Westrate, L.M., Lee, J.E., Prinz, W.A., and Voeltz, G.K. (2015). Form follows function: the importance of endoplasmic reticulum shape. *Annu. Rev. Biochem.* 84, 791–811. <https://doi.org/10.1146/annurev-biochem-072711-163501>.
2. Friedman, J.R., and Voeltz, G.K. (2011). The ER in 3D: a multifunctional dynamic membrane network. *Trends Cell Biol.* 21, 709–717. <https://doi.org/10.1016/j.tcb.2011.07.004>.
3. Bernales, S., McDonald, K.L., and Walter, P. (2006). Autophagy Counterbalances Endoplasmic Reticulum Expansion during the Unfolded Protein Response. *PLoS Biol.* 4, e423. <https://doi.org/10.1371/journal.pbio.0040423>.
4. Schuck, S., Prinz, W.A., Thorn, K.S., Voss, C., and Walter, P. (2009). Membrane expansion alleviates endoplasmic reticulum stress independently of the unfolded protein response. *J. Cell Biol.* 187, 525–536. <https://doi.org/10.1083/jcb.200907074>.
5. Walter, P., and Ron, D. (2011). The Unfolded Protein Response: From Stress Pathway to Homeostatic Regulation. *Science* 334, 1081–1086. <https://doi.org/10.1126/science.1209038>.
6. Hetz, C. (2012). The unfolded protein response: controlling cell fate decisions under ER stress and beyond. *Nat. Rev. Mol. Cell Biol.* 13, 89–102. <https://doi.org/10.1038/nrm3270>.
7. Hetz, C., Zhang, K., and Kaufman, R.J. (2020). Mechanisms, regulation and functions of the unfolded protein response. *Nat. Rev. Mol. Cell Biol.* 21, 421–438. <https://doi.org/10.1038/s41580-020-0250-z>.
8. Senft, D., and Ronai, Z.A. (2015). UPR, autophagy, and mitochondria crosstalk underlies the ER stress response. *Trends Biochem. Sci.* 40, 141–148. <https://doi.org/10.1016/j.tibs.2015.01.002>.
9. Travers, K.J., Patil, C.K., Wodicka, L., Lockhart, D.J., Weissman, J.S., and Walter, P. (2000). Functional and Genomic Analyses Reveal an Essential Coordination between the Unfolded Protein Response and ER-Associated Degradation. *Cell* 101, 249–258. [https://doi.org/10.1016/s0092-8674\(00\)80835-1](https://doi.org/10.1016/s0092-8674(00)80835-1).
10. Elgaard, L., and Helenius, A. (2003). Quality control in the endoplasmic reticulum. *Nat. Rev. Mol. Cell Biol.* 4, 181–191. <https://doi.org/10.1038/nrm1052>.
11. Brodsky, J.L. (2012). Cleaning Up: ER-Associated Degradation to the Rescue. *Cell* 151, 1163–1167. <https://doi.org/10.1016/j.cell.2012.11.012>.
12. Hartl, F.U., Bracher, A., and Hayer-Hartl, M. (2011). Molecular chaperones in protein folding and proteostasis. *Nature* 475, 324–332. <https://doi.org/10.1038/nature10317>.
13. Pobre, K.F.R., Poet, G.J., and Hendershot, L.M. (2019). The endoplasmic reticulum (ER) chaperone BiP is a master regulator of ER functions: Getting by with a little help from ERdj friends. *J. Biol. Chem.* 294, 2098–2108. <https://doi.org/10.1074/jbc.REV118.002804>.
14. Zuber, C., Cormier, J.H., Guhl, B., Santimaria, R., Hebert, D.N., and Roth, J. (2007). EDEM1 reveals a quality control vesicular transport pathway out of the endoplasmic reticulum not involving the COPII exit sites. *Proc. Natl. Acad. Sci. USA* 104, 4407–4412. <https://doi.org/10.1073/pnas.0700154104>.
15. Cui, Y., Parashar, S., Zahoor, M., Needham, P.G., Mari, M., Zhu, M., Chen, S., Ho, H.-C., Reggiori, F., Farhan, H., et al. (2019). A COPII subunit acts with an autophagy receptor to target endoplasmic reticulum for degradation. *Science* 365, 53–60. <https://doi.org/10.1126/science.aau9263>.

16. Fregno, I., Fasana, E., Bergmann, T.J., Raimondi, A., Loi, M., Soldà, T., Galli, C., D'Antuono, R., Morone, D., Danieli, A., et al. (2018). ER-to-lysosome-associated degradation of proteasome-resistant ATZ polymers occurs via receptor-mediated vesicular transport. *EMBO J.* 37, e99259. <https://doi.org/10.1525/embj.201899259>.
17. Duennwald, M.L., and Lindquist, S. (2008). Impaired ERAD and ER stress are early and specific events in polyglutamine toxicity. *Genes Dev.* 22, 3308–3319. <https://doi.org/10.1101/gad.1673408>.
18. Leitman, J., Ulrich Hartl, F., and Ledermann, G.Z. (2013). Soluble forms of polyQ-expanded huntingtin rather than large aggregates cause endoplasmic reticulum stress. *Nat. Commun.* 4, 2753. <https://doi.org/10.1038/ncomms3753>.
19. Abisambra, J.F., Jinwal, U.K., Blair, L.J., O'Leary, J.C., Li, Q., Brady, S., Wang, L., Guidi, C.E., Zhang, B., Nordhues, B.A., et al. (2013). Tau Accumulation Activates the Unfolded Protein Response by Impairing Endoplasmic Reticulum-Associated Degradation. *J. Neurosci.* 33, 9498–9507. <https://doi.org/10.1523/jneurosci.5397-12.2013>.
20. Balchin, D., Hayer-Hartl, M., and Hartl, F.U. (2016). In vivo aspects of protein folding and quality control. *Science* 353, aac4354. <https://doi.org/10.1126/science.aac4354>.
21. Stefani, M., and Dobson, C.M. (2003). Protein aggregation and aggregate toxicity: new insights into protein folding, misfolding diseases and biological evolution. *J. Mol. Med.* 81, 678–699. <https://doi.org/10.1007/s00109-003-0464-5>.
22. Aguzzi, A., and Altmeyer, M. (2016). Phase Separation: Linking Cellular Compartmentalization to Disease. *Trends Cell Biol.* 26, 547–558. <https://doi.org/10.1016/j.tcb.2016.03.004>.
23. Banani, S.F., Lee, H.O., Hyman, A.A., and Rosen, M.K. (2017). Biomolecular condensates: organizers of cellular biochemistry. *Nat. Rev. Mol. Cell Biol.* 18, 285–298. <https://doi.org/10.1038/nrm.2017.7>.
24. Bourdon, J.C., Renzing, J., Robertson, P.L., Fernandes, K.N., and Lane, D.P. (2002). Scotin, a novel p53-inducible proapoptotic protein located in the ER and the nuclear membrane. *J. Cell Biol.* 158, 235–246. <https://doi.org/10.1083/jcb.200203006>.
25. Kim, N., Kim, M.J., Sung, P.S., Bae, Y.C., Shin, E.C., and Yoo, J.Y. (2016). Interferon-inducible protein SCOTIN interferes with HCV replication through the autolysosomal degradation of NS5A. *Nat. Commun.* 7, 10631. <https://doi.org/10.1038/ncomms10631>.
26. Liu, Y., Yang, Y., Xu, C., Liu, J., Chen, J., Li, G., Huang, B., Pan, Y., Zhang, Y., Wei, Q., et al. (2023). Circular RNA circGli3 protects against islet β -cell dysfunction and apoptosis in obesity. *Nat. Commun.* 14, 351. <https://doi.org/10.1038/s41467-023-35998-z>.
27. Yun, H., Jung, M., Lee, H., Jung, S., Kim, T., Kim, N., Park, S.Y., Kim, W.J., Mun, J.Y., and Yoo, J.Y. (2023). Homotypic SCOTIN assemblies form ER-endosome membrane contacts and regulate endosome dynamics. *EMBO Rep.* 24, e56538. <https://doi.org/10.1525/embr.202256538>.
28. Kim, N., Kim, T.H., Kim, C., Lee, J.E., Kang, M.G., Shin, S., Jung, M., Kim, J.S., Mun, J.Y., Rhee, H.W., et al. (2023). Intrinsically disordered region-mediated condensation of IFN-inducible SCOTIN/SHISA-5 inhibits ER-to-Golgi vesicle transport. *Dev. Cell* 58, 1950–1966. <https://doi.org/10.1016/j.devcel.2023.08.030>.
29. Li, H., Korennykh, A.V., Behrman, S.L., and Walter, P. (2010). Mammalian endoplasmic reticulum stress sensor IRE1 signals by dynamic clustering. *Proc. Natl. Acad. Sci. USA* 107, 16113–16118. <https://doi.org/10.1073/pnas.1010580107>.
30. Liu, S., Zhang, X., Yao, X., Wang, G., Huang, S., Chen, P., Tang, M., Cai, J., Wu, Z., Zhang, Y., et al. (2024). Mammalian IRE1 α dynamically and functionally coalesces with stress granules. *Nat. Cell Biol.* 26, 917–931. <https://doi.org/10.1038/s41556-024-01418-7>.
31. Yoshida, H., Matsui, T., Yamamoto, A., Okada, T., and Mori, K. (2001). XBP1 mRNA Is Induced by ATF6 and Spliced by IRE1 in Response to ER Stress to Produce a Highly Active Transcription Factor. *Cell* 107, 881–891. [https://doi.org/10.1016/s0092-8674\(01\)00611-0](https://doi.org/10.1016/s0092-8674(01)00611-0).
32. Calfon, M., Zeng, H., Urano, F., Till, J.H., Hubbard, S.R., Harding, H.P., Clark, S.G., and Ron, D. (2002). IRE1 couples endoplasmic reticulum load to secretory capacity by processing the XBP-1 mRNA. *Nature* 415, 92–96. <https://doi.org/10.1038/415092a>.
33. Iwawaki, T., Akai, R., Kohno, K., and Miura, M. (2004). A transgenic mouse model for monitoring endoplasmic reticulum stress. *Nat. Med.* 10, 98–102. <https://doi.org/10.1038/nm970>.
34. Adams, S.R., Campbell, R.E., Gross, L.A., Martin, B.R., Walkup, G.K., Yao, Y., Llopis, J., and Tsien, R.Y. (2002). New biarsenical ligands and tetracycline motifs for protein labeling in vitro and in vivo: Synthesis and biological applications. *J. Am. Chem. Soc.* 124, 6063–6076. <https://doi.org/10.1021/ja017687n>.
35. Lam, S.S., Martell, J.D., Kamer, K.J., Deerinck, T.J., Ellisman, M.H., Moortha, V.K., and Ting, A.Y. (2015). Directed evolution of APEX2 for electron microscopy and proximity labeling. *Nat. Methods* 12, 51–54. <https://doi.org/10.1038/nmeth.3179>.
36. Bertolotti, A., Zhang, Y., Hendershot, L.M., Harding, H.P., and Ron, D. (2000). Dynamic interaction of BiP and ER stress transducers in the unfolded-protein response. *Nat. Cell Biol.* 2, 326–332. <https://doi.org/10.1038/35014014>.
37. Shen, J., Chen, X., Hendershot, L., and Prywes, R. (2002). ER Stress Regulation of ATF6 Localization by Dissociation of BiP/GRP78 Binding and Unmasking of Golgi Localization Signals. *Dev. Cell* 3, 99–111. [https://doi.org/10.1016/s1534-5807\(02\)00203-4](https://doi.org/10.1016/s1534-5807(02)00203-4).
38. Lai, C.W., Aronson, D.E., and Snapp, E.L. (2010). BiP availability distinguishes states of homeostasis and stress in the endoplasmic reticulum of living cells. *Mol. Biol. Cell* 21, 1909–1921. <https://doi.org/10.1091/mbc.E09-12-1066>.
39. Carrara, M., Prischl, F., Nowak, P.R., Kopp, M.C., and Ali, M.M. (2015). Noncanonical binding of BiP ATPase domain to Ire1 and Perk is dissociated by unfolded protein CH1 to initiate ER stress signaling. *Elife* 4, e03522. <https://doi.org/10.7554/elife.03522>.
40. Kopp, M.C., Nowak, P.R., Larburu, N., Adams, C.J., and Ali, M.M. (2018). In vitro FRET analysis of IRE1 and BiP association and dissociation upon endoplasmic reticulum stress. *Elife* 7, e30257. <https://doi.org/10.7554/elife.30257>.
41. Kopp, M.C., Larburu, N., Durairaj, V., Adams, C.J., and Ali, M.M.U. (2019). UPR proteins IRE1 and PERK switch BiP from chaperone to ER stress sensor. *Nat. Struct. Mol. Biol.* 26, 1053–1062. <https://doi.org/10.1038/s41594-019-0324-9>.
42. Rüdiger, S., Buchberger, A., and Bukau, B. (1997). Interaction of Hsp70 chaperones with substrates. *Nat. Struct. Biol.* 4, 342–349. <https://doi.org/10.1038/nsb0597-342>.
43. Mayer, M.P., and Bukau, B. (2005). Hsp70 chaperones: cellular functions and molecular mechanism. *Cell. Mol. Life Sci.* 62, 670–684. <https://doi.org/10.1007/s00018-004-4464-6>.
44. Marcinowski, M., Höller, M., Feige, M.J., Baerend, D., Lamb, D.C., and Buchner, J. (2011). Substrate discrimination of the chaperone BiP by autonomous and cochaperone-regulated conformational transitions. *Nat. Struct. Mol. Biol.* 18, 150–158. <https://doi.org/10.1038/nsmb.1970>.
45. Wieteska, L., Shahidi, S., and Zhuravleva, A. (2017). Allosteric fine-tuning of the conformational equilibrium poises the chaperone BiP for post-translational regulation. *Elife* 6, e29430. <https://doi.org/10.7554/elife.29430>.
46. Yang, J., Nune, M., Zong, Y., Zhou, L., and Liu, Q. (2015). Close and Allosteric Opening of the Polypeptide-Binding Site in a Human Hsp70 Chaperone BiP. *Structure* 23, 2191–2203. <https://doi.org/10.1016/j.str.2015.10.012>.
47. Zhuravleva, A., Clerico, E.M., and Giersch, L.M. (2012). An Interdomain Energetic Tug-of-War Creates the Allosterically Active State in Hsp70 Molecular Chaperones. *Cell* 151, 1296–1307. <https://doi.org/10.1016/j.cell.2012.11.002>.
48. Bertelsen, E.B., Chang, L., Gestwicki, J.E., and Zuiderweg, E.R.P. (2009). Solution conformation of wild-type *E. coli* Hsp70 (DnaK) chaperone

- complexed with ADP and substrate. *Proc. Natl. Acad. Sci. USA* 106, 8471–8476. <https://doi.org/10.1073/pnas.0903503106>.
49. Swain, J.F., Dinler, G., Sivendran, R., Montgomery, D.L., Stotz, M., and Gerasch, L.M. (2007). Hsp70 Chaperone Ligands Control Domain Association via an Allosteric Mechanism Mediated by the Interdomain Linker. *Mol. Cell* 26, 27–39. <https://doi.org/10.1016/j.molcel.2007.02.020>.
 50. Zhu, X., Zhao, X., Burkholder, W.F., Gragerov, A., Ogata, C.M., Gottesman, M.E., and Hendrickson, W.A. (1996). Structural Analysis of Substrate Binding by the Molecular Chaperone DnaK. *Science* 272, 1606–1614. <https://doi.org/10.1126/science.272.5268.1606>.
 51. Rosam, M., Krader, D., Nickels, C., Hochmair, J., Back, K.C., Agam, G., Barth, A., Zeymer, C., Hendrix, J., Schneider, M., et al. (2018). Bap (Sil1) regulates the molecular chaperone BiP by coupling release of nucleotide and substrate. *Nat. Struct. Mol. Biol.* 25, 90–100. <https://doi.org/10.1038/s41594-017-0012-6>.
 52. Xiao, X., Fay, A., Molina, P.S., Kovach, A., Glickman, M.S., and Li, H. (2024). Structure of the *M. tuberculosis* DnaK–GrpE complex reveals how key DnaK roles are controlled. *Nat. Commun.* 15, 660. <https://doi.org/10.1038/s41467-024-44933-9>.
 53. Shin, Y., Berry, J., Pannucci, N., Haataja, M.P., Toettcher, J.E., and Brangwynne, C.P. (2017). Spatiotemporal Control of Intracellular Phase Transitions Using Light-Activated optoDroplets. *Cell* 168, 159–171. <https://doi.org/10.1016/j.cell.2016.11.054>.
 54. Powers, E.T., and Balch, W.E. (2013). Diversity in the origins of proteostasis networks — a driver for protein function in evolution. *Nat. Rev. Mol. Cell Biol.* 14, 237–248. <https://doi.org/10.1038/nrm3542>.
 55. Bard, J.A.M., and Drummond, D.A. (2024). Chaperone regulation of biomolecular condensates. *Front. Biophys.* 2, 1342506. <https://doi.org/10.3389/fbri.2024.1342506>.
 56. Dea, A., and Pincus, D. (2024). The Heat Shock Response as a Condensate Cascade. *J. Mol. Biol.* 436, 168642. <https://doi.org/10.1016/j.jmb.2024.168642>.
 57. Chowdhary, S., Kainth, A.S., Paracha, S., Gross, D.S., and Pincus, D. (2022). Inducible transcriptional condensates drive 3D genome reorganization in the heat shock response. *Mol. Cell* 82, 4386–4399. <https://doi.org/10.1016/j.molcel.2022.10.013>.
 58. Zhang, H., Shao, S., Zeng, Y., Wang, X., Qin, Y., Ren, Q., Xiang, S., Wang, Y., Xiao, J., and Sun, Y. (2022). Reversible phase separation of HSF1 is required for an acute transcriptional response during heat shock. *Nat. Cell Biol.* 24, 340–352. <https://doi.org/10.1038/s41556-022-00846-7>.
 59. Ali, A., Garde, R., Schaffer, O.C., Bard, J.A.M., Husain, K., Kik, S.K., Davis, K.A., Luengo-Woods, S., Igarashi, M.G., Drummond, D.A., et al. (2023). Adaptive preservation of orphan ribosomal proteins in chaperone-dispersed condensates. *Nat. Cell Biol.* 25, 1691–1703. <https://doi.org/10.1038/s41556-023-01253-2>.
 60. Glauninger, H., Wong Hickernell, C.J., Bard, J.A.M., and Drummond, D.A. (2022). Stressful steps: Progress and challenges in understanding stress-induced mRNA condensation and accumulation in stress granules. *Mol. Cell* 82, 2544–2556. <https://doi.org/10.1016/j.molcel.2022.05.014>.
 61. Matsumoto, K., Minami, M., Shinozaki, F., Suzuki, Y., Abe, K., Zenno, S., Matsumoto, S., and Minami, Y. (2011). Hsp90 is involved in the formation of P-bodies and stress granules. *Biochem. Biophys. Res. Commun.* 407, 720–724. <https://doi.org/10.1016/j.bbrc.2011.03.088>.
 62. Suzuki, Y., Minami, M., Suzuki, M., Abe, K., Zenno, S., Tsujimoto, M., Matsumoto, K., and Minami, Y. (2009). The Hsp90 inhibitor geldanamycin abrogates colocalization of eIF4E and eIF4E-transporter into stress granules and association of eIF4E with eIF4G. *J. Biol. Chem.* 284, 35597–35604. <https://doi.org/10.1074/jbc.M109.036285>.
 63. Johnston, M., Geoffroy, M.C., Sobala, A., Hay, R., and Hutvagner, G. (2010). HSP90 protein stabilizes unloaded argonaute complexes and microscopic P-bodies in human cells. *Mol. Biol. Cell* 21, 1462–1469. <https://doi.org/10.1091/mbc.e09-10-0885>.
 64. Mediani, L., Antoniani, F., Galli, V., Vinet, J., Carrà, A.D., Bigi, I., Tripathy, V., Tiago, T., Cimino, M., Leo, G., et al. (2021). Hsp90-mediated regulation of DYRK3 couples stress granule disassembly and growth via mTORC1 signaling. *EMBO Rep.* 22, e51740. <https://doi.org/10.15252/embr.202051740>.
 65. Pedley, A.M., Boylan, J.P., Chan, C.Y., Kennedy, E.L., Kyoung, M., and Benkovic, S.J. (2022). Purine biosynthetic enzymes assemble into liquid-like condensates dependent on the activity of chaperone protein HSP90. *J. Biol. Chem.* 298, 101845. <https://doi.org/10.1016/j.jbc.2022.101845>.
 66. Gallagher, E.R., and Holzbaur, E.L.F. (2023). The selective autophagy adaptor p62/SQSTM1 forms phase condensates regulated by HSP27 that facilitate the clearance of damaged lysosomes via lysophagy. *Cell Rep.* 42, 112037. <https://doi.org/10.1016/j.celrep.2023.112037>.
 67. Lu, S., Hu, J., Arogundade, O.A., Goginashvili, A., Vazquez-Sanchez, S., Diedrich, J.K., Gu, J., Blum, J., Oung, S., Ye, Q., et al. (2022). Heat-shock chaperone HSPB1 regulates cytoplasmic TDP-43 phase separation and liquid-to-gel transition. *Nat. Cell Biol.* 24, 1378–1393. <https://doi.org/10.1038/s41556-022-00988-8>.
 68. Liu, Z., Zhang, S., Gu, J., Tong, Y., Li, Y., Gui, X., Long, H., Wang, C., Zhao, C., Lu, J., et al. (2020). Hsp27 chaperones FUS phase separation under the modulation of stress-induced phosphorylation. *Nat. Struct. Mol. Biol.* 27, 363–372. <https://doi.org/10.1038/s41594-020-0399-3>.
 69. Gu, J., Liu, Z., Zhang, S., Li, Y., Xia, W., Wang, C., Xiang, H., Liu, Z., Tan, L., Fang, Y., et al. (2020). Hsp40 proteins phase separate to chaperone the assembly and maintenance of membraneless organelles. *Proc. Natl. Acad. Sci. USA* 117, 31123–31133. <https://doi.org/10.1073/pnas.2002437117>.
 70. Boczek, E.E., Fursch, J., Niedermeier, M.L., Jawerth, L., Jahnel, M., Ruer-Gruss, M., Kammer, K.M., Heid, P., Mediani, L., Wang, J., et al. (2021). HspB8 prevents aberrant phase transitions of FUS by chaperoning its folded RNA-binding domain. *Elife* 10, e69377. <https://doi.org/10.7554/eLife.69377>.
 71. Shi, W., Ding, R., Chen, Y., Ji, F., Ji, J., Ma, W., and Jin, J. (2024). The HRD1-SEL1L ubiquitin ligase regulates stress granule homeostasis in couple with distinctive signaling branches of ER stress. *iScience* 27, 110196. <https://doi.org/10.1016/j.isci.2024.110196>.
 72. Chen, X., Shen, J., and Prywes, R. (2002). The Luminal Domain of ATF6 Senses Endoplasmic Reticulum (ER) Stress and Causes Translocation of ATF6 from the ER to the Golgi. *J. Biol. Chem.* 277, 13045–13052. <https://doi.org/10.1074/jbc.M110636200>.
 73. Schindelin, J., Arganda-Carreras, I., Frise, E., Kaynig, V., Longair, M., Pietzsch, T., Preibisch, S., Rueden, C., Saalfeld, S., Schmid, B., et al. (2012). Fiji: an open-source platform for biological-image analysis. *Nat. Methods* 9, 676–682. <https://doi.org/10.1038/nmeth.2019>.
 74. Harris, K.M., Spacek, J., Bell, M.E., Parker, P.H., Lindsey, L.F., Baden, A.D., Vogelstein, J.T., and Burns, R. (2015). A resource from 3D electron microscopy of hippocampal neuropil for user training and tool development. *Sci. Data* 2, 150046. <https://doi.org/10.1038/sdata.2015.46>.

STAR★METHODS

KEY RESOURCES TABLE

REAGENT or RESOURCE	SOURCE	IDENTIFIER
Antibodies		
BiP	Cell signaling technology	Cat# 3183; RRID: AB_10695864
BiP	Abcam	Cat# ab21685; RRID: AB_2119834
Caspase-8	Cell signaling technology	Cat# 9746; RRID: AB_2275120
CHOP	Cell signaling technology	Cat# 2895; RRID: AB_2089254
Cleaved Caspase-3	Cell signaling technology	Cat# 9661; RRID: AB_2341188
FLAG	Sigma	Cat# F1804; RRID: AB_262044
G3BP	BD Biosciences	Cat# 611126; RRID: AB_398437
GRP94	Atlas antibodies	Cat# AMAb91019; RRID: AB_2665765
Myc	Santa Cruz	Cat# sc-40; RRID: AB_2857941
Myc	Abcam	Cat# ab9106; RRID: AB_307014
Myc-Alexa Fluor 647	Cell signaling technology	Cat# 2233; RRID: AB_823474
Myc-FITC	Abcama	Cat# ab1263; RRID: AB_299270
Myc-FITC	Novus Biologicals	Cat# NB600-335F; RRID: AB_2936964
PARP1	Santa Cruz	Cat# sc-8007; RRID: AB_628105
PERK	Santa Cruz	Cat# sc-377400; RRID: AB_2762850
IRE1 (pSer724)	Novus biologicals	Cat# NB100-2323; RRID: AB_10145203
IRE1 α (B-12) AF594	Santa Cruz	Cat# sc-390960 AF594; RRID: AB_2936473
SCOTIN	Cusabio	Cat# CSB-PA818677LA01HU; RRID: AB_2936845
SCOTIN (C-7)	Santa Cruz	Cat# sc-390725; RRID: AB_2884032
Sec61 β	Atlas antibodies	Cat# HPA049407; RRID: AB_2680750
Vinculin	Santa Cruz	Cat# sc-55465; RRID: AB_630433
XBP1	Abcam	Cat# ab220783; RRID: AB_2920809
α -tubulin	Proteintech	Cat# 66031-1-Ig; RRID: AB_11042766
β -ACTIN	Santa Cruz	Cat# sc-1616; RRID: AB_2714189
IgG from mouse serum	Sigma	Cat# I8765; RRID: AB_1163672
HRP-mouse IgG	Thermo Fisher Scientific	Cat# 31430; RRID: AB_228307
HRP-rabbit IgG	Thermo Fisher Scientific	Cat# 31460; RRID: AB_228341
VeriBlot-HRP	Abcam	Cat# ab131366; RRID: AB_2892718
Donkey anti-rabbit IgG-Alexa 488	Invitrogen	Cat# A21206; RRID: AB_2535792
Donkey anti-rabbit IgG-Alexa 568	Invitrogen	Cat# A10042; RRID: AB_2534017
Donkey anti-rabbit IgG-Alexa 647	Invitrogen	Cat# A31573; RRID: AB_2536183
Donkey anti-mouse IgG-Alexa 488	Invitrogen	Cat# A21202; RRID: AB_141607
Donkey anti-mouse IgG-Alexa 568	Invitrogen	Cat# A10037; RRID: AB_2534013
Donkey anti-mouse IgG-Alexa 647	Invitrogen	Cat# A32787; RRID: AB_2762830
Chemicals, peptides, and recombinant proteins		
2,3-Dimercapto-1-propanol (BAL)	Sigma	Cat# 64046
2X Laemmli Buffer	Bio-Rad	Cat# 1610737
Aprotinin from bovine lung	Sigma	Cat# A6279
Benzamidine hydrochloride hydrate	Sigma	Cat# B6506
Bovine serum albumin	Biosesang	Cat# A1025
Bromophenol Blue	Thermo Fisher Scientific	Cat# BP115-25
Deoxycholic acid, Sodium Salt	Thermo Fisher Scientific	Cat# BP349-100
Dithiothreitol (DTT)	Sigma	Cat# D0632

(Continued on next page)

Continued

REAGENT or RESOURCE	SOURCE	IDENTIFIER
DMEM	Lonza	Cat# 12-604f
DMEM, high glucose, HEPES, no phenol red	Gibco	Cat# 21063029
DMSO	Sigma	Cat# D2650
Donkey serum	Sigma	Cat# D9663
Enhanced chemiluminescent (ECL)	Thermo Fisher Scientific	Cat# 34096
FBS	Welgene	Cat# S001-01
Fixation and Permeabilization Solution	BD bioscience	Cat# BD554722
Fluorescence mounting medium	Dako	Cat# S3023
Glycine	GENERAY Chemicals	Cat# 0167
Goat serum	Vector Laboratories	Cat# S1000
HBSS	Gibco	Cat# 14025-092
Recombinant Human IFN-γ	R&D Systems	Cat# 285-IF-100
Reverse Transcriptase	Promega	Cat# A3803
Leupeptin	Sigma	Cat# L2884
Lipofectamine 2000	Thermo Fisher Scientific	Cat# 11668019
MEM	Welgene	Cat# LM007-07
Nonidet P-40 Substitute	G-BIOSCIENCES	Cat# 786-512
NucBlue™ Fixed Cell ReadyProbes™ Reagent (DAPI)	Invitrogen	Cat# R37606
Oligo dT	Bioneer	Cat# N-7053
Paraformaldehyde	Thermo Fisher Scientific	Cat# A11313
PBS	Gibco	Cat# 21600-010
Pepstatin	Sigma	Cat# P4265
PMSF	Sigma	Cat# P7626
Polyethylenimine (PEI 25000)	Polysciences	Cat# 23966
Protein A/G agarose bead	Calbiochem	Cat# IP-10
Protein Assay Dye Reagent	Biorad	Cat# BR5000006
Puromycin dichydrochloride	AG Scientific	Cat# P-1033
ReAsH-EDT ₂	Cayman chemicals	Cat# 19767
RNAiso Plus	Takara	Cat# 9109
RNasin Ribonuclease Inhibitor	Promega	Cat# N2615
RPMI 1640	Welgene	Cat# LM011-03
Saponin	Sigma	Cat# 47036
Sodium Chloride	Thermo Fisher Scientific	Cat# BP358-10
Sodium dodecyl sulfate (SDS)	Sigma	Cat# L4509
Sodium fluoride	Sigma	Cat# S7920
Sodium orthovanadate	Sigma	Cat# S6508
Sucrose	Duchefa Biochemie	Cat# S0809
TB Green® Premix Ex Taq	Takara	Cat# RR420A
Thiazolyl Blue Tetrazolium Bromide (MTT)	Sigma	Cat# M5655
Thapsigargin	Sigma	Cat# T9033
Triton X-100	Thermo Fisher Scientific	Cat# BP151
Trizma base	Biosesang	Cat# T1016
Trypan Blue Solution	Welgene	Cat# LS014-01
Tunicamycin	Calbiochem	Cat# 654380
β-mercaptoethanol	Sigma	Cat# M6250
Experimental models: Cell lines		
293[HEK-293]	Korean Cell Line Bank	Cat# 21573
A-431	Korean Cell Line Bank	Cat# 21555

(Continued on next page)

Continued

REAGENT or RESOURCE	SOURCE	IDENTIFIER
A549	ATCC	Cat# CCL-185
DLD-1	Korean Cell Line Bank	Cat# 10221
HCT 116	Korean Cell Line Bank	Cat# 10247
HeLa	ATCC	Cat# CCL-2
HeLa SCOTIN knockout (KO)	This study	N/A
HepG2	ATCC	Cat# HB-8065
HT-29	Korean Cell Line Bank	Cat# 30038
Huh7	Korean Cell Line Bank	Cat# 60104
SW480	Korean Cell Line Bank	Cat# 10228
SW620	Korean Cell Line Bank	Cat# 60068
U-2 OS	Korean Cell Line Bank	Cat# 30096
Recombinant DNA		
SCOTIN	This study	N/A
SCOTIN-TC	This study	N/A
SCOTIN-MYC	This study	N/A
SCOTIN(Δ150-177)-MYC	This study	N/A
SCOTIN(Δ29-43)-MYC	This study	N/A
SCOTIN(Δ44-69)-MYC	This study	N/A
SCOTIN(Δ70-105)-MYC	This study	N/A
SCOTIN(Δ44-105)-MYC	This study	N/A
SCOTIN(Δ29-43,Δ70-105)-MYC	This study	N/A
SCOTIN(Δ29-69)-MYC	This study	N/A
SCOTIN(Δ29-43,Δ150-177)-MYC	This study	N/A
SCOTIN(Δ44-69,Δ150-177)-MYC	This study	N/A
SCOTIN(Δ70-105,Δ150-177)-MYC	This study	N/A
SCOTIN(Δ44-105,Δ150-177)-MYC	This study	N/A
SCOTIN(Δ29-43,Δ70-105,Δ150-177)-MYC	This study	N/A
SCOTIN(Δ29-69,Δ150-177)-MYC	This study	N/A
SCOTIN(ΔCRD)-MYC	This study	N/A
SCOTIN(ΔPRD)-MYC	This study	N/A
SCOTIN(ΔPRD+(150-177))-MYC	This study	N/A
SCOTIN(1-149)-MYC	This study	N/A
SCOTIN(1-177)-MYC	This study	N/A
SCOTIN(ΔPRD)-FUSN-MYC	This study	N/A
SCOTIN(1-149)-FUSN-MYC	This study	N/A
SCOTIN-APEX2	This study	N/A
mCherry-Cry2	This study	N/A
SCOTIN(CRD)-mCherry-Cry2	This study	N/A
3xFLAG-ATF6	Chen et al. ⁷²	Addgene #11975
IRE1-3F6HGFP	Peter Walter Lab (UCSF) ²⁹	N/A
F-XBP1ΔDBD-venus	Masayuki Miura (University of Tokyo) ³³	N/A
BiP-EGFP-KDEL	This study	N/A
BiP(K294F)-EGFP-KDEL	This study	N/A
BiP(V461F)-EGFP-KDEL	This study	N/A
BiP-(GGGGS) ₃ -mNeonGreen-KDEL	This study	N/A
SCOTIN gRNA/Cas9 knockout plasmid	Santa Cruz	Cat# sc-408226
SCOTIN HDR plasmid	Santa Cruz	Cat# sc-408226-HDR
Cre Vector	Santa Cruz	Cat# sc-418923

(Continued on next page)

Continued

REAGENT or RESOURCE	SOURCE	IDENTIFIER
Software and algorithms		
Adobe Illustrator	Adobe	https://www.adobe.com/products/illustrator.html
AlphaFold2	ColabFold	https://colab.research.google.com/github/sokrypton/ColabFold/blob/main/AlphaFold2.ipynb
cellSens	Olympus Life Science	https://www.olympus-lifescience.com/en/software/cellsens/
CSampler Plus	BD Biosciences	https://www.bd biosciences.com/en-us/products/instruments/flow-cytometers/clinical-cell-analyzers/facscalibur/csampler-plus-analysis-software-for-pc-or-mac.661084
Fiji (ImageJ)	Schindelin et al. (2012) ⁷³	https://fiji.sc
FV31S-SW	Olympus Life Science	https://www.olympus-lifescience.com/en/downloads/detail-iframe/?0[downloads][id]=847252002
PhotoZoom Pro 8	BenVista	https://www.benvista.com/photozoompro
PRISM	Graphpad	https://www.graphpad.com/scientific-software/prism/
PyMOL	Schrödinger	https://www.pymol.org/
Reconstruct	SynapseWeb	https://synapseweb.clm.utexas.edu/
Zen (blue edition)	Carl Zeiss Microscopy	https://www.zeiss.com/microscopy/en/products/software/zeiss-zen.html

EXPERIMENTAL MODEL AND STUDY PARTICIPANT DETAILS

Cell culture and transfection

HeLa, A549, and HepG2 cells were obtained from the American Type Culture Collection (ATCC). A-431, 293, DLD-1, HCT 116, HT-29, Huh7, SW480, SW620, and U-2 OS cells were obtained from Korean Cell Line Bank (KCLB). HeLa, A-431, A549, and 293 cells were grown in Dulbecco's modified Eagle's medium (DMEM; Lonza, 12-604f) supplemented with 10% fetal bovine serum (FBS; Biowest, A1025) at 37°C with 5% CO₂ in a humidified incubator. DLD-1, HCT 116, HT-29, Huh7, SW480, SW620, and U-2 OS cells were grown in RPMI 1640 medium (Welgene, LM011-03) supplemented with 10% FBS at 37°C with 5% CO₂ in a humidified incubator. HepG2 cells were grown in Minimum Essential Medium Eagle (MEM; Welgene, LM007-07) supplemented with 10% FBS at 37°C with 5% CO₂ in a humidified incubator. All cell lines were routinely tested and confirmed to be negative for mycoplasma contamination using a mycoplasma PCR detection kit (iNTRON, 25239). Plasmids were transfected with Lipofectamine 2000 (Life Technologies, 11668019) or polyethylenimine (PEI; Polysciences, 23966) for immunofluorescence staining and other experiments, respectively, according to the manufacturer's recommendations. Except for Figures 1A, S1A, and S1B, cells were fixed or harvested 24 h after transfection throughout the study.

SCOTIN knockout cell generation with CRISPR-Cas9-mediated genome editing

The SCOTIN knockout cell line was generated using the SCOTIN CRISPR-Cas9 knockout plasmid (Santa Cruz, sc-408226) and the HDR plasmid (Santa Cruz, sc-408226-HDR) following the manufacturer's protocol. HeLa cells were transfected with these two plasmids and cultured in medium supplemented with puromycin (1 mg/mL; AG Scientific, p-1033) until colonies grew. The depletion of endogenous SCOTIN in each colony was assessed by immunoblotting. A Cre vector (Santa Cruz, sc-418923) was used to excise the RFP/puromycin resistance gene flanked by the LoxP sites. Cells without RFP signals were sorted by flow cytometry and cultured in medium.

METHOD DETAILS

Plasmid construction

The coding sequence of full-length human SCOTIN (CCDS2770.1) was cloned and inserted into the pcDNA3.1/Myc-His A (Invitrogen, V80020) vector. To minimize the length of the protein tag, a stop codon was inserted downstream of the Myc epitope for a C-terminal Myc tag. A tetracycline (TC; FLNCCPGGCCMEP) sequence was inserted downstream of the SCOTIN sequence for a C-terminal TC tag. For the untagged SCOTIN plasmid, a stop codon was inserted between the SCOTIN sequence and the Myc epitope. SCOTIN

deletion mutants were generated via site-directed mutagenesis. To generate the chimeric constructs containing SCOTIN fused with FUSN, 1–214 aa of FUS cloned from pcDNA3.2-FUS-1-526aa-V5 (Addgene, 29609) were inserted downstream of the SCOTIN sequence. The coding sequence of full-length human BiP (CCDS6863.1) was cloned and inserted into the pEF-DEST51 (Invitrogen, 12285-011) vector. The EGFP or mNeonGreen sequence and the C-terminal KDEL sequence were inserted downstream of the BiP sequence. Point mutations in BiP were generated via site-directed mutagenesis. p3xFLAG-ATF6 (Addgene, 11975) was acquired from Addgene. The IRE1-3F6HGFP plasmid was generously provided by Dr. P. Walter (University of California, San Francisco). pCAX-F-XBP1ΔDBD-venus was generously provided by Dr. M. Miura (University of Tokyo). The optoDroplet plasmid (a gift from Yongdae Shin, Seoul National University) was subcloned and inserted into pcDNA3.1/Myc-His A (Invitrogen, V80020).

RNA isolation and reverse transcription-quantitative polymerase chain reaction (RT-qPCR)

Total RNA was extracted using RNAiso Plus (Takara, 9109). RNA was reverse transcribed using ImProm-II Reverse Transcriptase (Promega, A3803), RNasin Ribonuclease Inhibitor (Promega, N2615), and oligo dT primers (Bioneer, N-7053). Real-time PCR was performed using TB Green Premix Ex Taq (Takara, RR420A) with a StepOne Plus Real-Time PCR System (Applied Biosystems). Target gene expression was normalized to that of GAPDH. The sequences of the primers used were as follows: XBP-1s 5'-CTCATGGCCTTAGTTGAGAAC-3' and 3'-CTGCACCTGCTCGGGACTC-5'; CHOP, 5'-CTCCTGGAAATGAAGAGGAAGAAC-3' and 3'-CAGGGAGCTCTGACTGGAATC-5'; GRP78, 5'-AACTCCGGCGCGAGGTA-3' and 3'-GACCGGAACAGATCCATGTT-5'; and GAPDH, 5'-ATGGGGAAGGTGAAGGTGGAG-3' and 3'-GGAATCATATTGGAACATGTAAACCATGTAG-5'.

Immunoblotting

Cells were lysed in lysis buffer (25 mM Tris-Cl (pH 7.4), 150 mM NaCl, 1% Triton X-100, 0.5% deoxycholic acid, 0.1% SDS, 1 mM dithiothreitol (DTT), 1 mM benzamidine, 0.4 mM phenylmethylsulfonyl fluoride (PMSF), 10.4 μM pepstatin, 4 μg/mL aprotinin, and 1 μg/mL leupeptin) on ice for 30 min. For detection of phosphorylated proteins, 10 mM sodium fluoride and 10 mM sodium orthovanadate were added to the lysis buffer. The cell lysates were obtained via centrifugation of the supernatant at 13,000 rpm and 4°C for 20 min. The protein concentrations in the cell lysates were quantified using the Bradford method (Bio-Rad, BR5000006). The cell lysates were mixed with 5X protein loading buffer (15% sodium dodecyl sulfate (SDS), 0.825 M sucrose, 0.325 M Tris-Cl (pH 6.8), 0.002% bromophenol blue, and 5% β-mercaptoethanol) and heated at 95°C for 10 min. The proteins were separated on SDS-polyacrylamide gels and transferred to nitrocellulose membranes. The membranes were probed with primary antibodies followed by horseradish peroxidase (HRP)-conjugated secondary antibodies. The immunoreactive signals were detected using SuperSignal West Femto Maximum Sensitivity Substrate (Thermo Fisher Scientific, 34096) and visualized with an ImageQuant LAS 3000 (Fujifilm) or an ImageQuant LAS 4000 (GE Healthcare) imaging system.

Co-immunoprecipitation (coIP)

Cells were lysed in NP-40 lysis buffer (25 mM Tris-Cl (pH 7.4), 150 mM NaCl, 1% Nonidet P-40, 2 mM ethylenediaminetetraacetic acid (EDTA), 1 mM DTT, 1 mM benzamidine, 0.4 mM PMSF, 10.4 μM pepstatin, 4 μg/mL aprotinin, and 1 μg/mL leupeptin) at 4°C for 30 min with gentle rotation. The cell lysates were obtained via centrifugation of the supernatant at 13,000 rpm and 4°C for 20 min. The protein concentrations in the cell lysates were quantified using the Bradford method (Bio-Rad, BR5000006). The cell lysates were incubated with 1 μg of anti-mouse IgG (Sigma, I8765) or indicated primary antibody per 1 mg of cell lysate at 4°C overnight with gentle rotation. Protein A/G agarose beads (Calbiochem, IP10) were added for another 2 h of incubation with gentle rotation. The beads were washed with NP-40 lysis buffer five times, and proteins were eluted from the beads by incubation with 2X Laemmli sample buffer (Bio-Rad, BR1610737) supplemented with 5% β-mercaptoethanol at 95°C for 10 min.

Immunostaining for fluorescence microscopy

Cells were washed with PBS three times and fixed with 4% paraformaldehyde (Thermo Fisher Scientific, A11313) at room temperature (RT) for 10 min and were then incubated with blocking buffer (0.3 M glycine, 10% goat serum or 10% donkey serum, 1% bovine serum albumin (BSA), and 0.2% saponin in PBS) at RT for 1 h. The cells were incubated with primary antibodies in buffer (1% BSA and 0.2% saponin in PBS) at 4°C overnight and were then incubated with Alexa Fluor 488-, 568-, or 647-conjugated secondary antibodies in PBST (0.1% Tween 20 in PBS) at RT for 1 h. To visualize nuclei, NucBlue Fixed Cell ReadyProbes Reagent (Invitrogen, R37606) was used. The coverslips were mounted with fluorescence mounting medium (Dako, S3023). Images were acquired using a 60× objective lens with an FLUOVIEW FV3000 confocal microscope (Olympus) or a 63× objective lens with an LSM900 confocal microscope with Airyscan 2 (Carl Zeiss). The laser power and fluorescence intensities of each channel were identical for each sample in a single experiment, except for Nucleus.

FRAP assay

Cells were cultured in 35-mm glass bottom dishes (Cellvis, D35-20-1-N). To visualize the cells expressing SCOTIN-TC, ReAsH-EDT₂ (Cayman Chemicals, 19767) dye was used. The cells were washed with HBSS (Gibco, 14025-092) twice and incubated with HBSS containing 2 μM ReAsH-EDT₂ for 1 h at 37°C with 5% CO₂ in a humidified incubator. Then, the cells were washed and incubated with HBSS containing 250 μM 2,3-dimercapto-1-propanol (BAL; Sigma, 64046) for 5 min at 37°C with 5% CO₂ in a humidified incubator. After washing with HBSS, the cells were incubated with phenol red-free DMEM (Gibco, 21063029) supplemented with 10% FBS

during live cell imaging. Images were acquired using a $60\times$ objective lens with a FLUOVIEW FV3000 confocal microscope (Olympus). For the FRAP analysis, the selected regions of SCOTIN-TC puncta or BiP-mNG-KDEL puncta were bleached using a 561 nm laser at 100% power for 3 s or a 488 nm laser at 100% power for 10 s, respectively. The control regions were areas of the same size within the same cell where no bleaching event occurred. Fluorescence recovery was monitored by image acquisition at intervals of 5.34 s for SCOTIN-TC and 4.8 s for BiP-mNG-KDEL. The fluorescence intensities of the photobleached region and control region were measured using cellSens software (Olympus LS). The fluorescence intensities of the photobleached regions were normalized to the intensities of the same region before photobleaching (photobleaching effect) and to those of the control regions at the same time point (autobleaching effect during recording). The recovery half-time ($t_{1/2}$) and the plateau were calculated by nonlinear regression and the “plateau followed by one-phase association” model in GraphPad Prism software (version 10.2.0).

Correlative light and electron microscopy (CLEM) and 3D reconstruction

For CLEM and 3D reconstruction, HeLa cells were grown to 30–40% confluence in 35-mm glass grid-bottomed culture dishes (MatTek Life Science, P35G-1.5-14-CGRD). Next, the cells were transfected with SCOTIN-TC using Lipofectamine 2000 (Thermo Fisher Scientific, 11668019). The next day, the cells were fixed with 2.5% glutaraldehyde (Electron Microscopy Sciences, 16200) and 2% paraformaldehyde (Electron Microscopy Sciences, 19210) in a 0.1 M cacodylate solution (pH 7.0) for 1 h. After washing, the cells were stained with ReAsH-EDT₂ dye. The stained cells were imaged under a confocal light microscope (Ti-RCP; Nikon, Japan), and images were obtained with the exact cell position on the MatTek grid in the differential interference contrast (DIC) channel. After confocal imaging, the stained cells were postfixed in 2% osmium tetroxide (OsO_4) containing 1.5% potassium ferrocyanide for 1 h at 4°C. The fixed cells were dehydrated through an ethanol series (50%, 60%, 70%, 80%, 90%, and 100%) by incubation for 10 min at each concentration and infiltrated with embedding medium. After embedding, 60 nm sections were sliced horizontal to the plane of the block (UC7; Leica Microsystems, Germany) and mounted on copper slot grids with a specimen support film. Then, the sections were double-stained with UranyLess (Electron Microscopy Sciences, 22409) for 2 min and 3% lead citrate (Electron Microscopy Sciences, 22410) for 1 min. The sections were then observed using a Tecnai G2 transmission electron microscope (Thermo Fisher Scientific, USA) at 120 kV. Confocal micrographs were produced as high-quality large images using PhotoZoom Pro 8 software (Benvista Ltd., Houston, TX, USA). Enlarged fluorescence images were fitted to the electron micrographs using ImageJ and the BigWarp plugin. For 3D reconstruction, serial images were aligned using the image processing package Fiji and the plugin TrackEM2.⁷³ After alignment, 3D reconstructions were generated manually by Reconstruct software.⁷⁴

Transmission electron microscopy (TEM)

To observe the DAB-stained cells, HeLa cells were transfected with the control empty vector or SCOTIN-APEX2 plasmid using Lipofectamine 2000 (Thermo Fisher Scientific, 11668019). The next day, the cells were fixed with 1% glutaraldehyde (Electron Microscopy Sciences, 16200) and 1% paraformaldehyde (Electron Microscopy Sciences, 19210) in 0.1 M cacodylate solution (pH 7.0) for 1 h at 4°C. After washing, 20 mM glycine solution was used to quench the unreacted aldehydes. 3,3'-Diaminobenzidine (DAB, Sigma, D8001) staining was performed for approximately 20–40 min until a light-brown stain was visible under an inverted light microscope. DAB-stained cells were postfixed with 2% osmium tetroxide in distilled water for 30 min at 4°C, stained *en bloc* in 1% uranyl acetate (EMS, USA, 22400) overnight and dehydrated through a graded ethanol series. The samples were then embedded with an EMBed-812 embedding kit (Electron Microscopy Sciences, 14120) and polymerized in an oven at 60°C. The polymerized samples were sectioned (60 nm) with an ultramicrotome (UC7; Leica Microsystems, Germany), and the sections were mounted on copper slot grids with a specimen support film. Sections were stained with UranyLess (Electron Microscopy Sciences, 22409) and lead citrate (Electron Microscopy Sciences, 22410) and were then examined with a Tecnai G2 transmission electron microscope (Thermo Fisher Scientific, USA).

Flow cytometry

Cells were detached and resuspended in medium. Equal numbers of cells were washed with FACS buffer (2% FBS in PBS) and collected by centrifugation at 900 rpm at 4°C for 5 min. The cells were treated with Cytofix/Cytoperm Fixation and Permeabilization Solution (BD Biosciences, BD554722) at RT for 10 min followed by three washes with FACS buffer containing 0.1% saponin and 1% BSA. Then, the cells were stained with an Alexa 647-conjugated anti-Myc antibody at RT for 1 h. After washing with FACS buffer three times, the cells were resuspended in 500 µL of FACS buffer and then analyzed using a BD Accuri C6 Plus flow cytometer (BD Biosciences).

MTT assay

Cells were cultured in a 24-well culture plate. At the indicated times after transfection, the cells were incubated with 0.5 mg/mL MTT (Sigma, M5655) in PBS at 37°C for 3 h. After removing the MTT solution, the cells were incubated with isopropanol:DMSO (9:1) solution at 37°C for 15 min. The reaction solution was transferred to a 96-well plate, and the absorbance was measured at 562 nm and 650 nm (reference) using a Spark multimode microplate reader (Tecan).

optoDroplet assay

Cells were cultured in a 60-mm culture dish. At 24 h after transfection, the cells were treated with phenol red-free DMEM (Gibco, 21063029) supplemented with 10% FBS for live cell imaging. Images were acquired using a 40 \times objective and a TCS SP5 confocal microscope (Leica). The intracellular distribution of the SCOTIN CRD was examined using a 561 nm laser following activation with a 488 nm laser at 5% power. Cells exhibiting optoDroplet formation were quantified.

Protein structure prediction using AlphaFold2

For protein structure prediction of SCOTIN-BiP complex, AlphaFold2 (ColabFold v1.5.5) was utilized. The protein sequences of SCOTIN (NP_057563.3) and BiP (NP_005338.1) without signal sequences (SCOTIN; 1–28 aa, BiP; 1–18 aa) were inputted into query sequence. The PyMOL Molecular Graphics System (version 3.1.1) was used to label each domain with different colors for the predicted structures.

QUANTIFICATION AND STATISTICAL ANALYSIS

For colocalization analysis by immunostaining, the boundary of each cell was defined in DIC images to determine the region of interest (ROI). The colocalization degree was calculated with Fiji (ImageJ) software and the plugin Coloc2. For densitometric analysis of the immunoblots, protein band intensities were measured using Fiji (ImageJ) software. All the statistical analyses were performed using GraphPad Prism (version 10.2.0). Statistical significance was calculated by a two-tailed unpaired t test. The lines and error bars in the graph indicate the means \pm standard deviations (SDs). Significance was defined as follows: * p value < 0.05, ** p value < 0.01, *** p value < 0.001, **** p value < 0.0001, and n.s. (not significant), p value > 0.05.